The Astronomical Journal, 165:203 (28pp), 2023 May https://doi.org/10.3847/1538-3881/acc6ca

The Orbital and Physical Properties of Five Southern Be+sdO Binary Systems

Luqian Wang (王璐茜)[1,2,4], Douglas R. Gies[2,4], Geraldine J. Peters[3], and Zhanwen Han[1]
[1] Yunnan Observatories, Chinese Academy of Sciences (CAS), Kunming 650216, Yunnan, People's Republic of China; wangluqian@ynao.ac.cn, zhanwenhan@ynao.ac.cn
[2] Center for High Angular Resolution Astronomy and Department of Physics and Astronomy, Georgia State University, P.O. Box 5060, Atlanta, GA 30302-5060, USA; dgies@gsu.edu
[3] Department of Physics and Astronomy, University of Southern California, Los Angeles, CA 90089-0484, USA; gpeters@usc.edu
Received 2022 November 12; revised 2023 March 19; accepted 2023 March 21; published 2023 April 18

Abstract

Close binary interactions may play a critical role in the formation of the rapidly rotating Be stars. Mass transfer can result in a mass gainer star spun up by the accretion of mass and angular momentum, while the mass donor is stripped of its envelope to form a hot and faint helium star. Far-UV spectroscopy has led to the detection of about 20 such binary Be+sdO systems. Here we report on a 3 yr program of high-quality spectroscopy designed to determine the orbital periods and physical properties of five Be binary systems. These binaries are long orbital period systems with P = 95–237 days and small semiamplitude $K_1 < 11$ km s^{-1}. We combined the Be star velocities with prior sdO measurements to obtain mass ratios. A Doppler tomography algorithm shows the presence of the He II $\lambda 4686$ line in the faint spectrum of the hot companion in four of the targets. We discuss the observed line variability and show evidence of phase-locked variations in the emission profiles of HD 157832, suggesting a possible disk spiral density wave due to the presence of the companion star. The stripped companions in HD 113120 and HD 137387 may have a mass larger than 1.4 $M_\odot$, indicating that they could be progenitors of Type Ib and Ic supernovae.

Unified Astronomy Thesaurus concepts: Stellar evolution (1599); Spectroscopic binary stars (1557); Emission line stars (460)

Supporting material: machine-readable tables

1. Introduction

The Be stars are B-type main-sequence stars whose spectra show or have shown Balmer emission lines. Such emission features probably originate in a circumstellar decretion disk around the central star. The exact formation mechanism of the disk is not clear, but it is widely accepted that the disk is geometrically thin and moving in Keplerian motion governed by viscosity (Quirrenbach et al. 1997; Meilland et al. 2007; Rivinius et al. 2013). The Be stars often display photometric and spectroscopic line variations, and such variability spans timescales from days to months (Hanuschik et al. 1996; Arcos et al. 2018). They are rapid rotators, and their projected rotational velocities can reach up to ~80% of their critical rotational velocities (Rivinius et al. 2013).

Some theoretical studies suggest that single Be stars may spin up due to physical changes at certain evolutionary stages. These processes include the transportation of angular momentum from the central contracting core to the outer envelope (Meynet et al. 2007), the effects of large initial rotational velocity and nonsolar metallicity (Ekström et al. 2008), and the influence of equatorial mass loss for the near-critical rotation of Be stars (Granada et al. 2013).

Alternatively, close binary interactions offer another way to understand the rapid rotation of Be stars and, consequently, the Be phenomenon. Pols et al. (1991) and van Bever & Vanbeveren (1997) performed calculations for Case B close binary evolution and concluded that a nonnegligible fraction of the Be population was formed through close binary interactions. In such a binary scenario, the initially more massive star loses its outer hydrogen envelope and transfers mass to the gainer star through Roche-lobe overflow. The mass and angular momentum transfer process may rejuvenate and spin up the gainer star, which now appears as a rapidly rotating Be star. The former donor star becomes an evolved remnant, such as a black hole, neutron star, or helium subdwarf star (sdO). Recent binary population synthesis (BPS) simulations from Shao & Li (2014, 2021) indicate that Be+sdO binary systems are abundant in the Milky Way with an estimated number of order 10^4. Using various assumptions for the mass ratio distribution and mass transfer efficiency, these authors suggested that Be+sdO binaries likely have orbital periods from 80 to 200 days, helium companion masses from 0.3 to 0.6 $\mathcal{M}_\odot^N$ (nominal solar value[5]), and Be star semiamplitudes of ~8 km s^{-1}.

Despite the large number of Be+sdO binaries predicted from theoretical simulations, only a handful of such systems are found observationally. The first known Be+sdO binary system, ϕ Per, was detected through optical spectroscopy of the antiphase motion of the He II $\lambda 4686$ emission line formed in hot gas near the sdO star (Poeckert 1981). The spectral

---

[4] Visiting astronomer, Cerro Tololo Inter-American Observatory at NSF's NOIRLab, which is managed by the Association of Universities for Research in Astronomy (AURA) under a cooperative agreement with the National Science Foundation.

[5] The superscript N indicates the nominal values of the solar units that are the standard values set forth by the International Astronomical Union at the XXIXth General Assembly (Prša et al. 2016). They are recommended for usage in stellar and planetary publications for a homogeneous unit system to avoid inconsistent conversion constants appearing in the SI unit transformation.

signature of the sdO star itself was subsequently confirmed from the International Ultraviolet Explorer (IUE) far-UV (FUV) spectral analysis by Thaller et al. (1995). The physical and orbital properties of this system were later determined by Gies et al. (1998) using observations from Hubble Space Telescope (HST) FUV spectroscopy and by Mourard et al. (2015) using near-IR interferometry from the CHARA Array. Because the sdO stars are hotter than their Be primaries, identifying their spectral features is best accomplished in the FUV, since they contribute relatively more flux toward the short-wavelength part of the spectrum. Studies from IUE FUV spectroscopy led to detection of sdO companions in Be binaries FY CMa (Peters et al. 2008), 59 Cyg (Peters et al. 2013), HR 2142 (Peters et al. 2016), and 60 Cyg (Wang et al. 2017). Later assessment of available FUV observations for a sample of 264 stars in the IUE database by Wang et al. (2018) led to the detection of an additional 12 Be+sdO candidate binary systems, and the spectral signature of the sdO stars in nine of them was later confirmed by HST FUV spectroscopy (Wang et al. 2021). The subdwarf stars in these Be+sdO binary systems have effective temperatures ($T_{\rm eff}$) in the range from 34 to 53 kK, small projected rotational velocities $V \sin i < 36$ km s^{-1} (with the exception of $V \sin i = 102 \pm 4$ km s^{-1} in the case of HD 51354; Wang et al. 2021), flux ratios $f_{\rm sdO}/f_{\rm Be}$ between 1% and about 10%, small radii $R_{\rm sdO} < 0.6\ \mathcal{R}_\odot^{\rm N}$, low luminosity $\log L_{\rm sdO} < 4.1\ \mathcal{L}_\odot^{\rm N}$, orbital periods of 28–126 days, and estimated masses of 0.1–1.0 $\mathcal{M}_\odot^{\rm N}$. However, the masses and orbital parameters of these hot subdwarf stars remain poorly constrained due to the limited number of FUV spectra.

Although it is difficult to identify the spectral features of the sdO star from optical spectroscopy due to the faintness and small size compared to the Be star, indirect evidence indicating the detection of sdO stars is reported in several works. Chojnowski et al. (2018) utilized high-quality optical observations to trace the signature of the sdO companion in the HD 55606 binary system from the He II λ4686 profile appearing in the spectra. Studies of the He I λ6678 emission profile revealed possible sdO companions in the cases of o Pup (Koubský et al. 2012), HD 161306 (Koubský et al. 2014), and 7 Vul (Harmanec et al. 2020). Furthermore, periodic V/R variations appearing in the violet and red emission peaks of the He I λ6678 profile in o Pup may also indicate its binary nature (Rivinius et al. 2012). Recently, Nazé et al. (2022) conducted a radial velocity (RV) monitoring survey for 16 γ Cas–type stars with strong X-ray emission, and they reported that these systems likely harbor a small mass companion (0.6–1.0 $\mathcal{M}_\odot^{\rm N}$) in orbits with long periods (80–120 days). Harmanec et al. (2022) performed a comprehensive study to investigate the spectral, photometric, and color variations of V1294 Aql using observations spanning about 70 yr, and they concluded that this is likely another Be+sdO binary candidate system. An extensive analysis of archival optical spectra and new CHARA Array interferometry of κ Dra by Klement et al. (2022a) suggest the existence of a cooler subdwarf companion (sdB) in this Be binary.

Long-term monitoring programs of the Be+sdO binary systems to determine their orbits and stellar parameters are vital to tracing their evolutionary history. Direct comparison of the measured quantities to models will provide constraints on the nature of these binary systems, such as evaluating the dynamic stability of the binaries based upon the critical mass ratio of the system, estimating the mass-loss or accretion state of the component stars, investigating the mass-stripping process, and tracing their formation efficiency (Shao & Li 2014, 2021). Investigating the physical properties of the Be binaries provides insights into understanding the formation and rapid rotation features of massive stars (de Mink et al. 2013). Stripped hot stars are also important contributors to the ionizing flux of stellar populations (Götberg et al. 2019). Massive subdwarf stars may explode as Type Ib and Ic supernovae (SNe Ib and Ic; Laplace et al. 2021; Aguilera-Dena et al. 2022) and leave compact neutron star (Reig 2011) or black hole (Schneider et al. 2021) remnants.

Motivated by the recent detection of hot subdwarf stars in Be+sdO binary systems from FUV spectroscopy by Wang et al. (2021), we conducted a long-term optical spectroscopic monitoring program to measure RVs and determine the orbital and physical parameters. Here we report on the first part of the work that is focused on five Be+sdO binary systems visible in the southern sky. In Section 2, we describe the observations. Section 3 presents the line profiles identified in the optical spectra of each target star, the RV measurements made from strong lines, and the derivation of the orbital elements. We document the line profile variations and emission line equivalent widths in Section 4. Section 5 summarizes our use of Doppler tomography to detect the He II λ4686 absorption profile from the sdO companion stars. We present in Section 6 a comparison of the physical and orbital properties with those of known Be+sdO (sdB) binary systems, and we give a brief discussion of the theoretical aspects of the formation of such Be binaries. We offer our conclusions in Section 7.

2. Spectroscopy Program

The spectra of five southern Be targets were obtained with the high resolving power echelle spectrometer CHIRON installed on the Small and Moderate Aperture Research Telescope System 1.5 m telescope at the Cerro Tololo Inter-American Observatory in Chile. The spectra were collected between 2018 April 23 and 2021 July 23 through the queue observing mode using the image slicer with a spectral resolving power $R = 80{,}000$. The spectra are recorded in 59 echelle orders covering a wavelength range from 4150 to 8800 Å (Tokovinin et al. 2013). Table 1 lists the HD number, star name, Hipparcos HIP number, V-band magnitude, spectral classification and associated reference, number of observations, and UT date range for each target star. These stars were identified as Be+sdO systems through FUV spectroscopic detection of the sdO line patterns (Wang et al. 2018, 2021). One of the stars, HD 137387, was identified as a spectroscopic binary system based upon the analysis from Jilinski et al. (2010), but the rest of the stars in the list were not previously known binaries. Appendix D provides a summary of recent studies of these stars.

The spectra were reduced following the standard reduction procedures, including bias subtraction, flat-field correction, removal of cosmic rays, echelle order extraction, and wavelength calibration through the usage of Th–Ar lamps (Paredes et al. 2021). The spectra are dominated by broad Balmer lines associated with the Be star disk, and these often span more than one echelle order. Consequently, we adopted the technique from Kolbas et al. (2015) to use the flux in adjoining orders to remove the blaze function variation in orders recording the broad features. Because the atmospheric telluric lines were not removed from the observed spectra, we

Table 1
Spectroscopic Program Targets

HD Number	Star Name	HIP Number	V (mag)	Spectral Classification	References	Number of Spectra	UT Date Range
113120	LS Mus	63688	6.03	B2 IVne	1	45	2018 Apr 23–2021 Apr 18
137387	κ Aps	76013	5.49	B2 Vnpe	1	46	2019 Jan 12–2021 Jul 13
152478	V846 Ara	82868	6.33	B3 Vnpe	1	49	2019 Feb 21–2021 Jul 20
157042	ι Ara	85079	5.25	B2.5 IVe	2	47	2019 Feb 23–2021 Jul 18
157832	V750 Ara	85467	6.66	B1.5 Ve	3	47	2019 Feb 26–2021 Jul 23

References. (1) Levenhagen & Leister (2006), (2) Slettebak (1982), (3) Lopes de Oliveira & Motch (2011).

thus adopted the atmospheric transmission spectral library by Hinkle et al. (2003) to correct for these absorption features. We applied a fitting scheme to identify the telluric absorption lines by matching the observations with the atmospheric transmission profiles and subsequently removed these features from the observed spectra. We then transformed the spectra onto a uniform wavelength grid on a log λ scale with a step size of 2.26 km s^{-1} pixel^{-1}, and we rectified the spectra to a unit continuum from selected continuum points in relatively line-free regions. The final working products are matrix arrays of normalized flux as a function of heliocentric wavelength and heliocentric corrected Julian date (HJD) for each echelle order.

3. RVs and Orbital Elements

In order to determine the orbital solutions of these Be+sdO binary systems, we first inspected the spectra to identify suitable line profiles for measurement of the RVs of the Be component. Below, we describe the selected spectral features and the detailed procedures for RV measurements of each star.

3.1. HD 113120

The spectra of HD 113120 contain emission line profiles of the Balmer series, including Hα and Hβ, He I lines, and metallic lines (including Fe II, Si II, and the Ca II triplet series). The metallic line profiles, such as Si II and the Ca II triplet, as well as the He I profiles, are generally too weak to make reliable RV measurements. The He I $\lambda\lambda$5875, 6678, 7065 and Hβ profiles display line variations that affect the line wings (see Section 4.1). Thus, we restrict the Be component's RV measurements to the echelle spectral orders containing the Hα, Hβ, and Fe II profiles only. The Hα profile is very broad and displays emission peak variations (see Figure 11 below). Porter & Rivinius (2003) suggested that the Be disks rotate with Keplerian motion, so the high-speed wings are likely formed close to the Be stars. Thus, measurements of the Doppler shifts of the line wings provide a good proxy for the orbital motion of the Be star. We adopted the wing bisector technique from Shafter et al. (1986) to use two oppositely signed Gaussian functions to sample the wings of the profile to determine the bisector position and measure the velocity of the Be star. We adopted the derivations from Grundstrom (2007; her Appendix A.2) to estimate the error of the RV measurements from samplings of the spectral flux, separation of the two Gaussian functions, and the uncertainties in the continuum. An example of the Hα profile observed on the night of HJD 2,458,482 with the associated RV measurement is shown in Figure 1. Alternatively, we utilized a calculation of the cross-correlation function (CCF) of the observed spectra with the coadded mean spectrum to measure the relative RVs for the Hβ and Fe II profiles ($\lambda\lambda$5276, 5316, 5362, 8451). These ancillary RV measurements are included in Table B1 of Appendix B.

Similar to other known Be binary systems (e.g., Harmanec et al. 2000, 2002), the RVs measured from the Hα wings of HD 113120 display long-term variations on a timescale of about a year that are most likely due to the variations in the emission profiles caused by structural changes in the disk. We thus applied corrections to the measured Doppler shifts to remove such long-term variations. The detailed procedures are discussed in Appendix A. Table 2 lists the star name, observational date, derived orbital phase from the SB2 solution, corrected RV and associated error, derived residual velocity, and line profile used to measure the Doppler shift for each observation of the five target stars. The RV measurements and orbital solutions for the other four target stars are discussed in the following subsections.

We applied a global minimization convergence method developed by Iglesias-Marzoa et al. (2015) to obtain the orbital solution using the RV measurements made from the Hα profile. These include the orbital period, the epoch when the Be star reaches superior conjunction in its orbit, the semiamplitude of the velocity curves and the systemic velocity of each component star, eccentricity, and the longitude of periastron of the fitting orbit. Equal weight was assigned to each velocity measurement for the orbital fitting, except in the case of the spectrum obtained on the night of HJD 2,458,232, in which a zero weight was given because the measured RV deviated greatly from the derived orbital solution. This spectrum showed a steep drop in intensity, and the profile displayed a redshift compared to the adjacent spectrum in the data set observed about 250 days later. We found no improvements in the fit residuals by adopting an eccentric orbital solution; thus, we report the derived single-lined, circular orbital elements in the second column of Table 3.

Wang et al. (2018, 2021) performed an FUV spectral analysis of this star and reported RV measurements for the sdO companion obtained from IUE and HST observations. We utilized these measurements to derive the orbital solutions for both stellar components, and the best-fit RV curves are shown in red in Figure 2. The RV measurements made from the high-resolution HST spectra ($R = 45{,}800$; blue) achieve a better velocity fit compared to those of lower-resolution IUE observations ($R = 13{,}000$; green). We give the derived circular orbital solutions from both components in the third column of Table 3. Note that the uncertainties quoted for the different parameters are the internal errors from the fitting routine (Iglesias-Marzoa et al. 2015), and these do not account for systematic errors introduced in the corrections procedure for long-term trends (Appendix A). The RV curves for the Hβ and

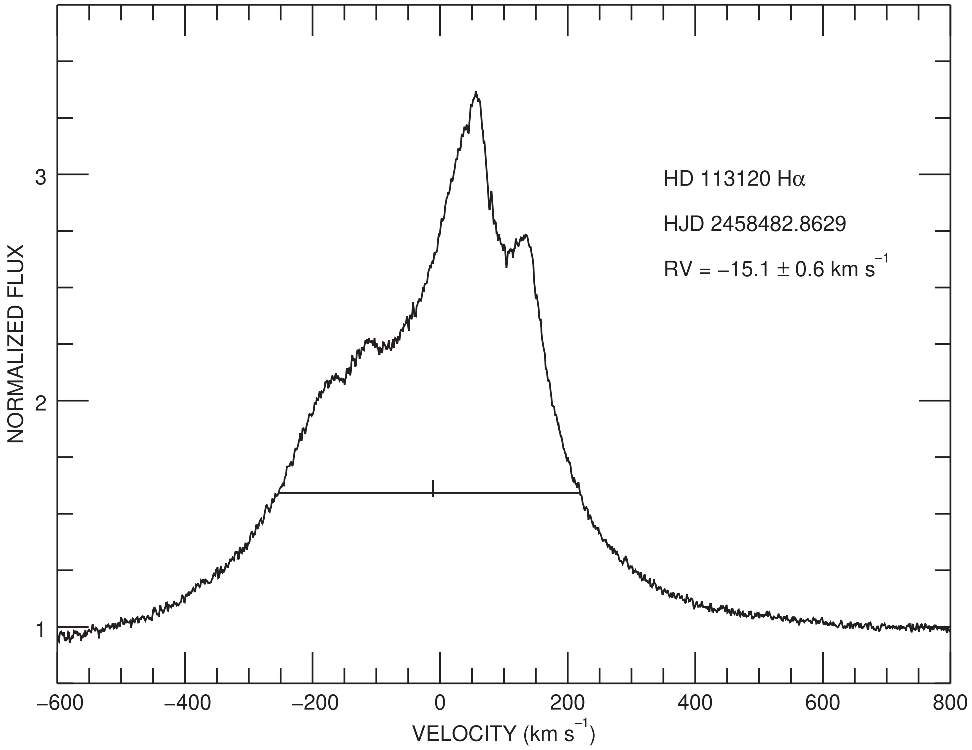

Figure 1. Example of the Hα profile observed on the night of HJD 2,458,482 for HD 113120. The horizontal line indicates 25% of the peak height of the profile, and two oppositely signed Gaussian functions were located at the intersection points to sample the wings of the profile and determine the bisector position of the Doppler shift (shown as the tick mark).

Table 2
RV Measurements of the Be Stars

HD Number	Date (HJD−2,400,000)	Orbital Phase[a]	V_r (km s^{-1})	σ_r (km s^{-1})	$O-C$ (km s^{-1})	Line Measured[b]
113120	58,232.6079[c]	0.012	−3.9	1.0	⋯	Hα
113120	58,482.8629	0.392	−15.1	0.6	4.1	Hα
113120	58,486.8532	0.414	−16.6	0.6	1.4	Hα
113120	58,495.8407	0.463	−13.3	0.6	1.7	Hα
113120	58,497.8571	0.474	−15.6	1.0	−1.3	Hα

Notes.

[a] The orbital phase of each measurement is obtained from the SB2 fits of the associated target star, except in the case of HD 157832, in which the orbital phases are from the SB1 fit.

[b] Hα profiles were used to measure the RVs of the target stars, except for the case of HD 137387, where the He I λ5875 profile was chosen for measurement.

[c] The RV measured from this spectrum was given a zero weight and excluded from the orbital fit due to its large deviation from the derived orbital solution.

(This table is available in its entirety in machine-readable form.)

Fe II profiles plotted using the derived SB2 ephemeris are shown in Appendix Figure B2.

3.2. HD 137387

The spectra of HD 137387 are dominated by broad and strong Balmer line profiles, including the Hα and Hβ profiles (see panel (a) of Figure 12 in Section 4.2). The Hα line displays profile variations transitioning from a broad absorption feature (observed on the night of HJD 2,458,540) to a narrower absorption superimposed on top of a wide emission profile (HJD 2,459,409), indicating an ongoing disk development in this Be star. Such variations prevent us from obtaining reliable RV measurements from the Hα profiles.

Instead, we measured RVs for the Be star from echelle orders containing Hβ and He I λλ4713, 4921, 5015, 5875, 6678, 7065 absorption lines by calculating the CCFs of the observed spectra with their coadded mean spectrum. The calculated CCFs are very broad, as expected from the rapid rotation of the Be star. We thus determined the Doppler shifts of the star from the wing bisector position of the CCFs as described in Section 3.1, except in the case of He I λ5875, where the CCF peak velocities were obtained (using the correction constants listed in Table A1 of Appendix A). Figure 3 shows an example of the He I λ5875 profile observed on the night of HJD 2,458,482 (black) and the coadded mean spectrum (green). The measured relative RV is shown as the tick mark in the figure. The RV measurements made from the He I profiles generally have too much scatter to make a reliable orbital fit, except for the case of He I λ5875, in which the best orbital RV curve was achieved with a circular fit of the measurements (Figure 4). We report the derived single-lined orbital solution of the star in the second column of Table 4.

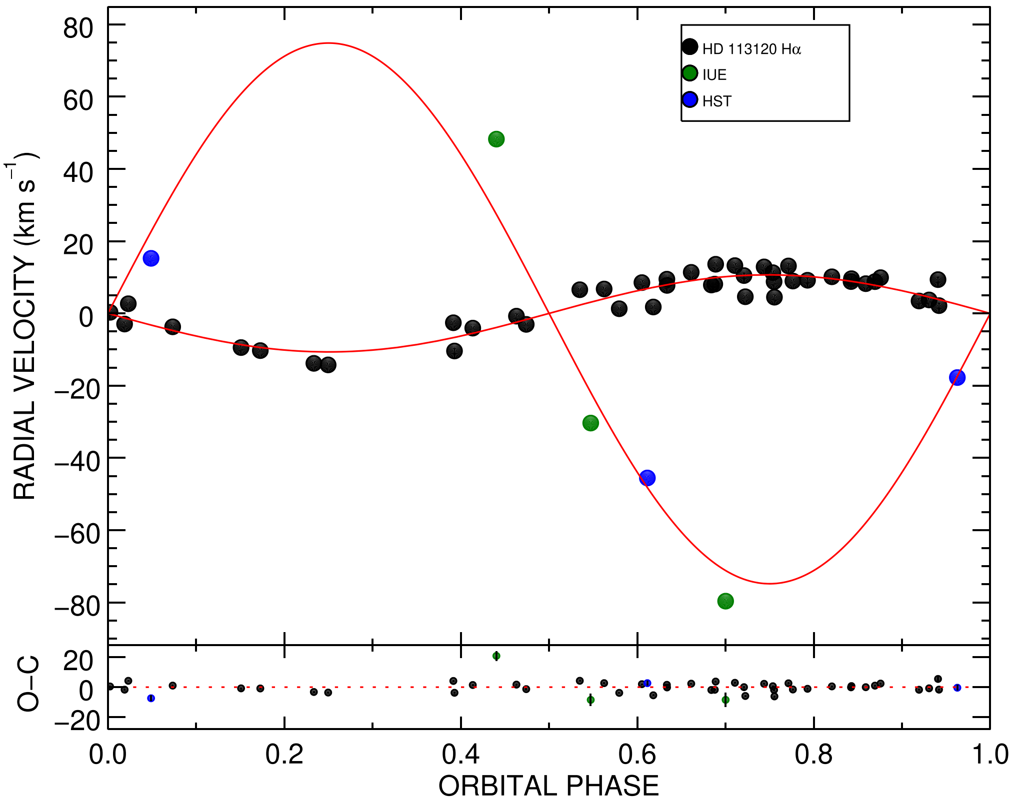

Figure 2. Top panel: relative RV curves (red) for the Be+sdO binary system HD 113120. The zero orbital phase is defined as the epoch when the Be star reaches superior conjunction in its orbit. The RVs of the Be star measured from the CHIRON Hα profiles are labeled with black dots, and the RVs of the sdO companion star obtained from the prior studies using FUV spectroscopy from IUE (Wang et al. 2018) and HST (Wang et al. 2021) are shown in green and blue, respectively. Systemic velocities for each stellar component obtained from the orbital fits were subtracted from individual measurements for the purposes of this plot. Bottom panel: measured RVs minus the calculated values obtained from the orbital fits. The zero residuals are shown as the red dotted line. The typical error of the measured Be RVs is ∼0.5 km s^{-1}, which is too small to be shown in the figure.

Prior FUV spectroscopy of this binary system by Wang et al. (2018, 2021) led to seven measurements of RVs for the sdO companion star (four from IUE and three from HST). Thus, we also determined a preliminary circular orbital solution using RVs for both stellar components, and the results are reported in the third column of Table 4. The RV curves with double-lined orbital fits are shown in Figure 4. The corrected relative RVs and their associated errors from measurements of the He I λ5875 profiles are listed in Table 2 together with the orbital phases and residuals from the double-lined solution, and five RV measurements made between HJD 2,458,526 and HJD 2,458,544 were assigned a zero weight due to their large deviations from the orbital fits. The RV measurements made from Hβ and the other He I line profiles are reported in Table B3 of Appendix B.

Table 3
Circular Orbital Elements of HD 113120

Element	Value	
	SB1	SB2
P (days)	183.40 ± 0.15	181.54 ± 0.11
$T_{\rm sc}$ (HJD−2,400,000)	58,591.96 ± 0.13	58,593.32 ± 0.13
K_1 (km s^{-1})	10.89 ± 0.06	10.66 ± 0.03
K_2 (km s^{-1})	⋯	74.8 ± 0.4
q	⋯	0.142 ± 0.001
γ_1 (km s^{-1})	−12.68 ± 0.06	−12.52±0.03
γ_2 (km s^{-1})	⋯	15.56 ± 0.26
$f(m_1)$ ($\mathcal{M}_\odot^{\rm N}$)	0.0246 ± 0.0004	0.0228 ± 0.0002
$f(m_2)$ ($\mathcal{M}_\odot^{\rm N}$)	⋯	7.88 ± 0.13
$a_1 \sin i$ ($\mathcal{R}_\odot^{\rm N}$)	39.48 ± 0.22	38.23 ± 0.10
$a_2 \sin i$ ($\mathcal{R}_\odot^{\rm N}$)	⋯	268.4 ± 1.5
$a \sin i$ ($\mathcal{R}_\odot^{\rm N}$)	⋯	306.7 ± 1.9
$M_1 \sin^3 i$ ($\mathcal{M}_\odot^{\rm N}$)	⋯	10.29 ± 0.21
$M_2 \sin^3 i$ ($\mathcal{M}_\odot^{\rm N}$)	⋯	1.47 ± 0.04
rms$_1$ (km s^{-1})	2.6	2.7
rms$_2$ (km s^{-1})	⋯	10.3

3.3. HD 152478

The spectra of HD 152478 display weak He I absorption features and strong double-peaked emission features in the Balmer profiles of Hα and Hβ. The strengths of the violet and red Hα emission peaks varied throughout the observations (see panel (a) of Figure 13 in Section 4.3). Broad weak absorption profiles of He I (including λλ4713, 4921, 5875, 6678, 7065) and weak metallic emission features of Fe II λ8451 and Ca II λ8542 appear in the spectra but are too weak to obtain reliable Doppler shift measurements. We measured the Doppler shifts of the Be star from the broad Hα wings using the bisector technique. Systematic shifts appear in the measured RVs for observations obtained after HJD 2,458,800, and long-term corrections were applied to the RVs as discussed in Appendix A. Figure 5 shows an example of the Hα profile observed on HJD 2,458,536, and the determined bisector location is marked on the plot to indicate the RV measurement. We report the corrected RVs and the associated errors for Hα in the fourth and fifth columns of Table 2. We tested both a

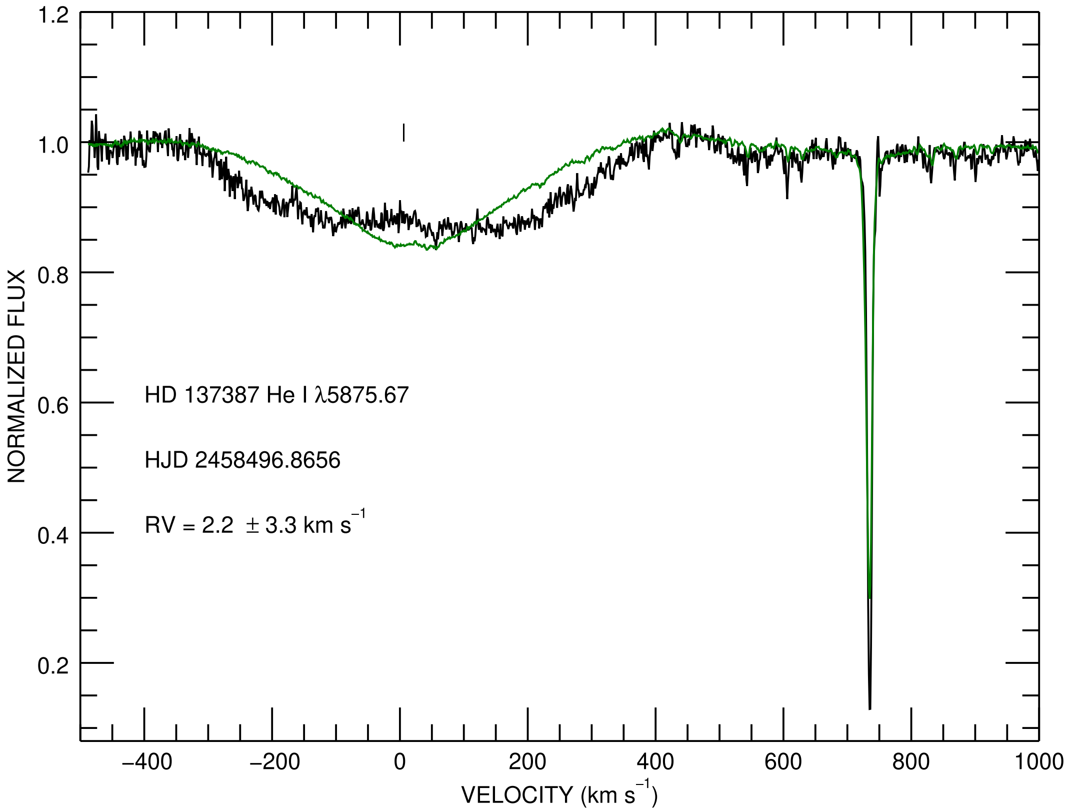

Figure 3. The He I λ5875 profile observed on the night of HJD 2,458,496 (black) and the coadded mean spectrum (green) for HD 137387. The relative RV (2.2 ± 3.3 km s^{-1}; shown as the tick mark) was measured from the peak position of the CCF that was calculated by cross-correlating the observed spectrum with the mean spectrum of all 46 observations.

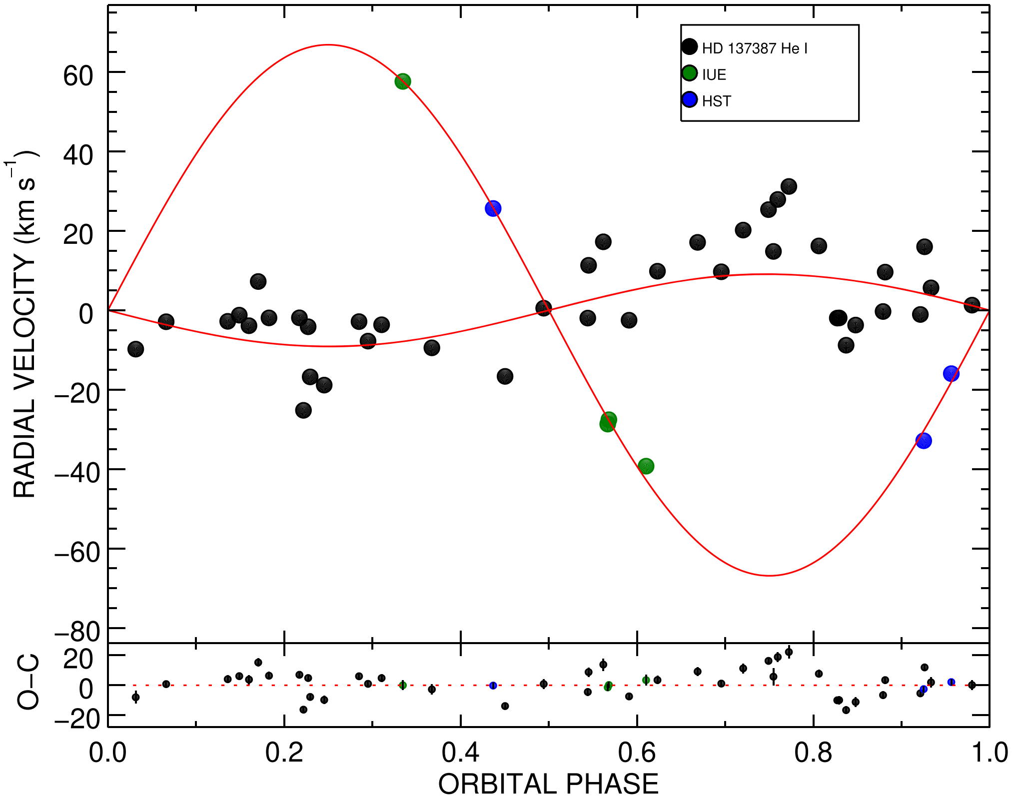

Figure 4. Relative RV curves for the Be binary HD 137387, plotted in the same format as Figure 2. The RVs of the Be star were measured from the He I λ5875 profiles using the cross-correlation technique.

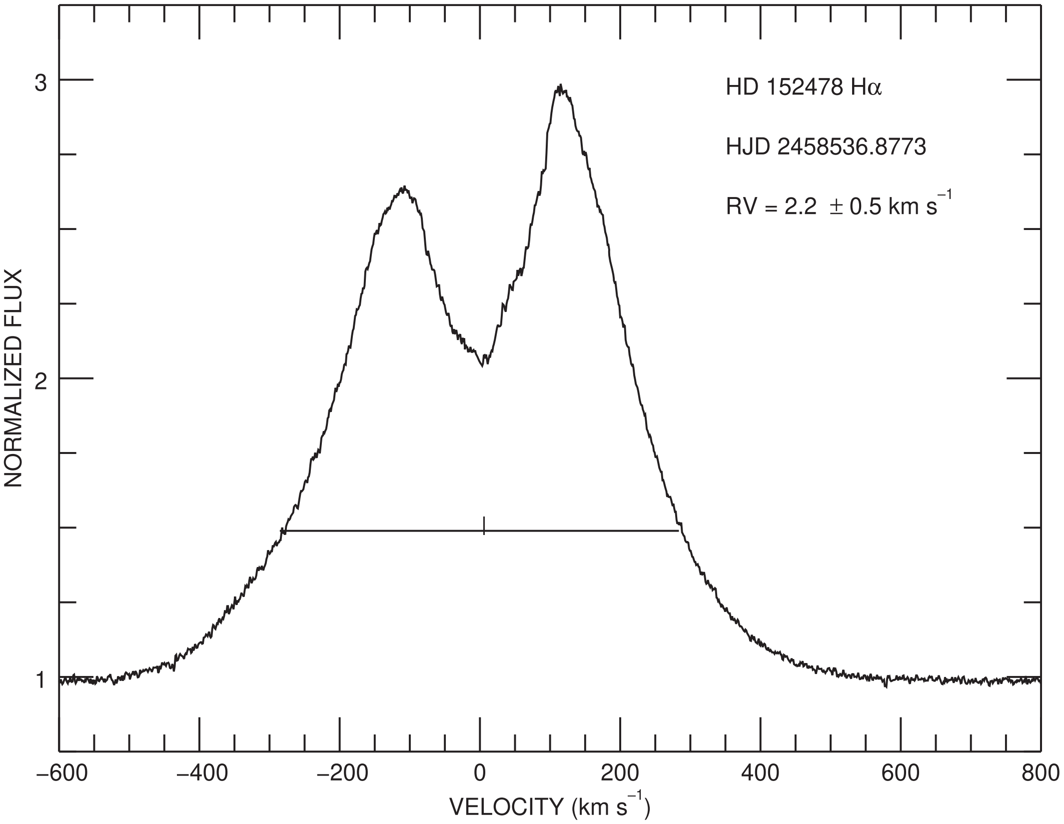

Figure 5. The Hα profile observed on the night of HJD 2,458,536 for HD 152478. The RV measured from the broad wings using the bisector technique is shown as the tick mark.

Table 4
Circular Orbital Elements of HD 137387

Element	Value	
	SB1	SB2
P (days)	191.9 ± 0.3	192.1 ± 0.1
$T_{\rm sc}$ (HJD−2,400,000)	58,402.4 ± 2.4	58,401.9 ± 2.2
K_1 (km s^{-1})	9.08 ± 0.11	9.09 ± 0.08
K_2 (km s^{-1})	⋯	66.87 ± 1.84
q	⋯	0.136 ± 0.004
γ_1 (km s^{-1})[a]	1.66 ± 0.12	1.67 ± 0.08
γ_2 (km s^{-1})	⋯	15.46 ± 0.99
$f(m_1)$ ($\mathcal{M}_{\odot}^{\rm N}$)	0.0149 ± 0.0006	0.0150 ± 0.0004
$f(m_2)$ ($\mathcal{M}_{\odot}^{\rm N}$)	⋯	5.95 ± 0.49
$a_1 \sin i$ ($\mathcal{R}_{\odot}^{\rm N}$)	34.5 ± 0.4	34.5 ± 0.3
$a_2 \sin i$ ($\mathcal{R}_{\odot}^{\rm N}$)	⋯	253.8 ± 7.0
$a \sin i$ ($\mathcal{R}_{\odot}^{\rm N}$)	⋯	288.3 ± 8.4
$M_1 \sin^3 i$ ($\mathcal{M}_{\odot}^{\rm N}$)	⋯	7.7 ± 0.7
$M_2 \sin^3 i$ ($\mathcal{M}_{\odot}^{\rm N}$)	⋯	1.0 ± 0.1
rms$_1$ (km s^{-1})	9.6	9.6
rms$_2$ (km s^{-1})	⋯	1.9

Note.
[a] Based upon relative RVs.

Table 5
Circular Orbital Elements of HD 152478

Element	Value	
	SB1	SB2
P (days)	236.12 ± 0.20	236.50 ± 0.18
$T_{\rm sc}$ (HJD−2,400,000)	58,672.25 ± 0.74	58,672.10 ± 0.72
K_1 (km s^{-1})	4.31 ± 0.06	4.33 ± 0.05
K_2 (km s^{-1})	⋯	52.83 ± 1.49
q	⋯	0.082 ± 0.003
γ_1 (km s^{-1})	5.63 ± 0.07	5.60 ± 0.06
γ_2 (km s^{-1})	⋯	10.15 ± 1.22
$f(m_1)$ ($\mathcal{M}_{\odot}^{\rm N}$)	0.0020 ± 0.0001	0.0020 ± 0.0001
$f(m_2)$ ($\mathcal{M}_{\odot}^{\rm N}$)	⋯	3.62 ± 0.30
$a_1 \sin i$ ($\mathcal{R}_{\odot}^{\rm N}$)	20.1 ± 0.3	20.2 ± 0.2
$a_2 \sin i$ ($\mathcal{R}_{\odot}^{\rm N}$)	⋯	247.0 ± 6.9
$a \sin i$ ($\mathcal{R}_{\odot}^{\rm N}$)	⋯	267.2 ± 8.2
$M_1 \sin^3 i$ ($\mathcal{M}_{\odot}^{\rm N}$)	⋯	4.23 ± 0.42
$M_2 \sin^3 i$ ($\mathcal{M}_{\odot}^{\rm N}$)	⋯	0.35 ± 0.05
rms$_1$ (km s^{-1})	2.6	2.6
rms$_2$ (km s^{-1})	⋯	0.1

circular and an eccentric orbital fit to the measured RVs and found that the circular solution achieves an adequate fit (given in the second column of Table 5).

Five FUV observations were obtained from prior investigations (two IUE and three HST), and we used these to determine a preliminary double-lined orbital solution (third column of Table 5). The derived orbital phases and calculated $O-C$ residuals obtained from the double-lined circular orbit fit are listed in the third and sixth columns, respectively, of Table 2. In Figure 6, we show the circular orbital fits and measured RVs of the Be component and the sdO companion star.

We also measured RVs for Hβ but used a different approach. We formed CCFs of each profile with the global average profile and then measured the bisector position for the wings of the

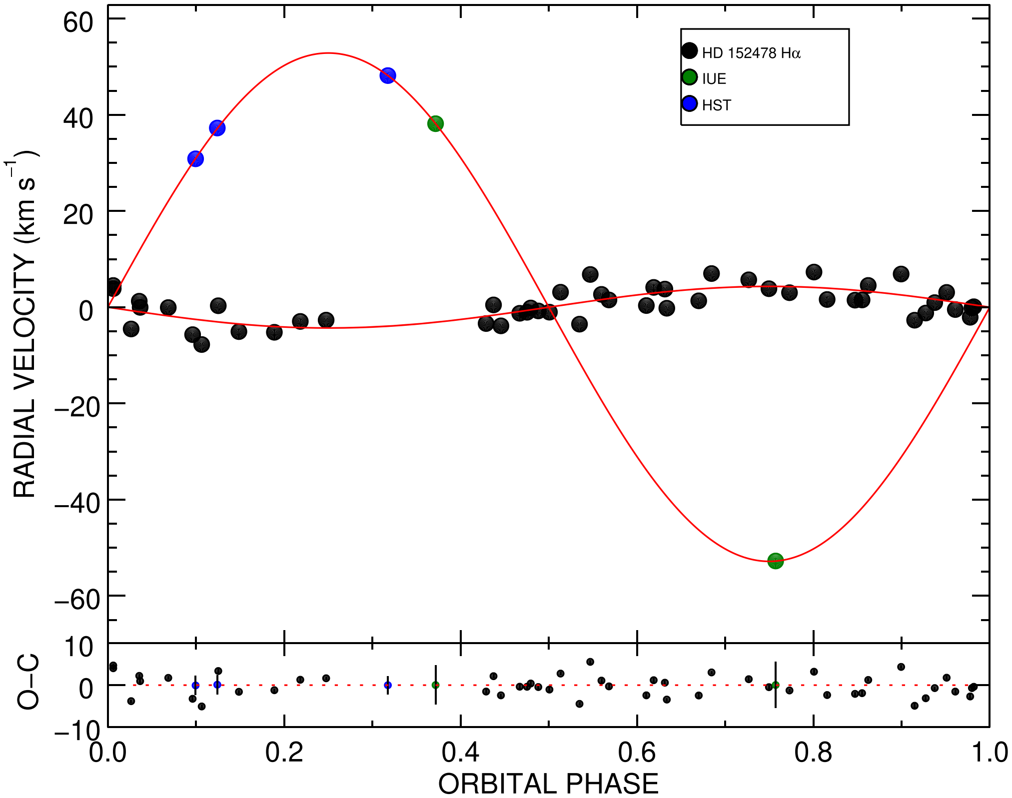

Figure 6. Relative RV curves for the Be binary HD 152478, plotted in the same format as Figure 2. The RVs of the Be star were measured from the Hα profiles using the bisector technique. The sdO RVs are collected from prior studies by Wang et al. (2018, 2021).

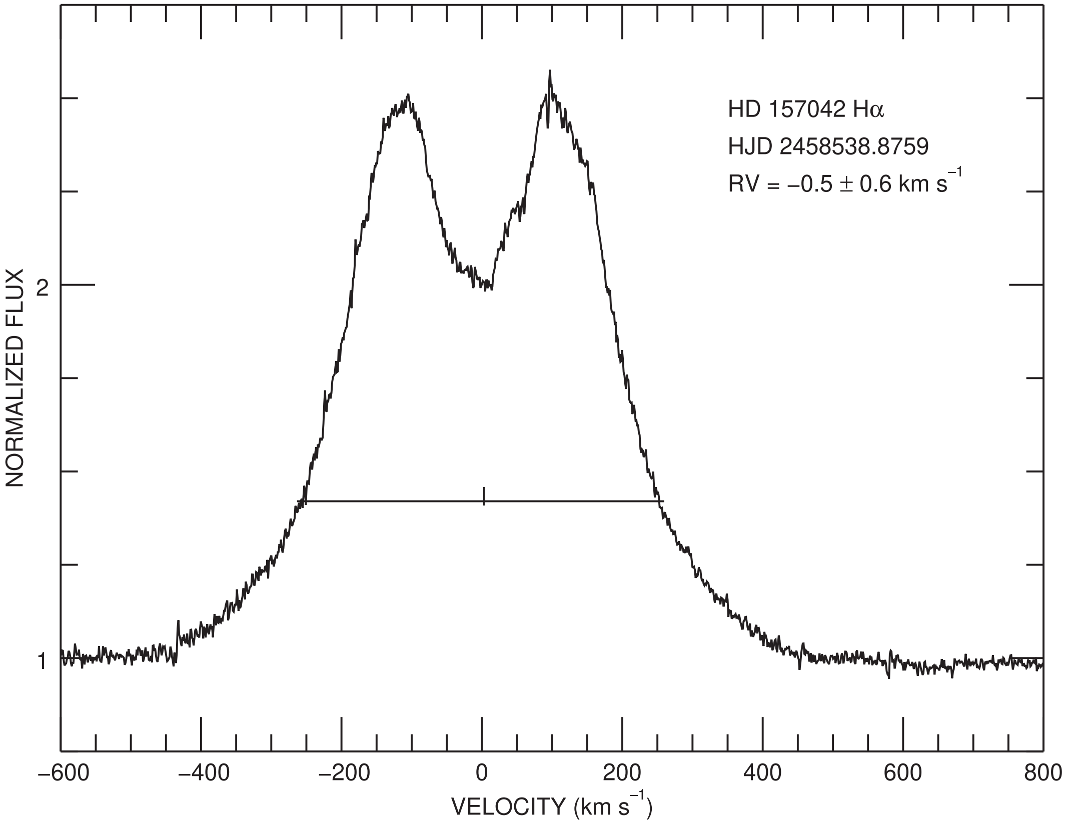

Figure 7. The Hα profile of HD 157042 observed on the night of HJD 2,458,538. The RV measured from the broad wings using the bisector technique is shown as the tick mark.

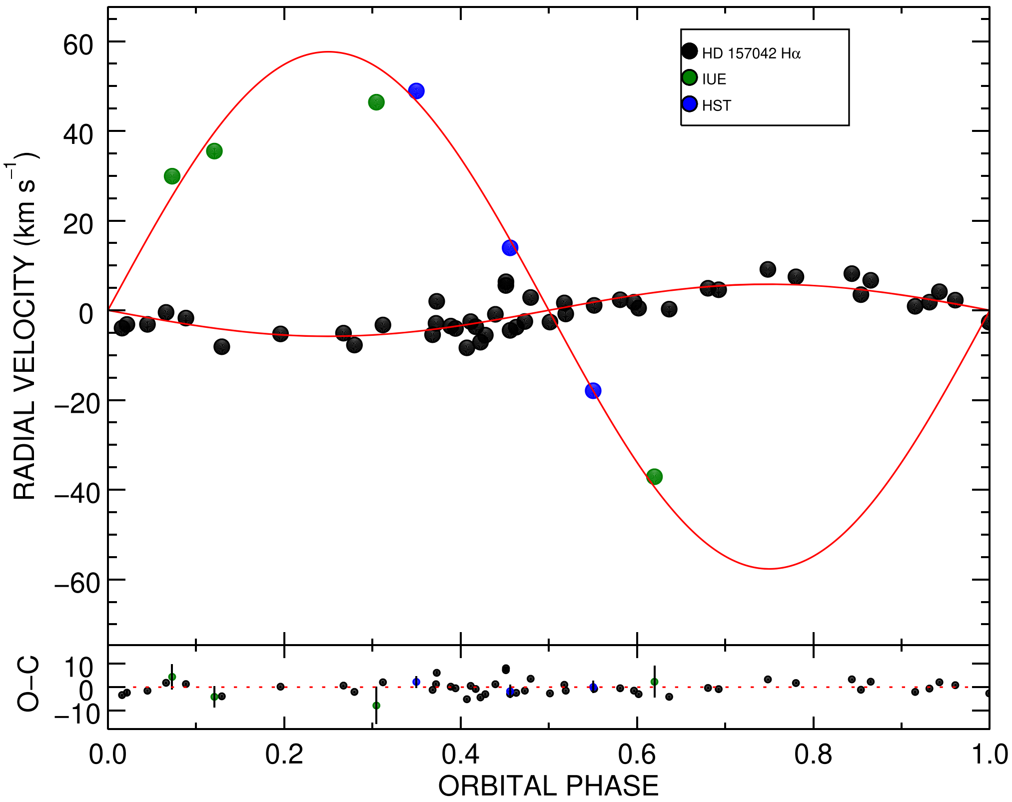

Figure 8. Relative RV curves for HD 157042 in the same format as Figure 2.

CCFs. These relative velocities are listed in Table 5 and plotted versus the orbital phase from the double-lined ephemeris in panel (a) of Figure B3 in Appendix B. The relative velocities for Hβ have a similar appearance to the RV curve for Hα but with greater scatter.

3.4. HD 157042

The optical spectra of HD 157042 are dominated by double-peaked emission features appearing in Balmer profiles of Hα and Hβ lines (see panel (a) of Figure 14 in Section 4.4). Broad weak absorption lines of He I $\lambda\lambda$4713, 4921, 5015, 5875, 6678, 7065 and metallic emission features such as Fe II $\lambda\lambda$8451, 8490 and Ca II $\lambda\lambda$8542, 8600 appear in the spectra. We again measured the RVs of the Be star from the broad Hα wings using the Gaussian-sampled bisector method. Figure 7 shows an example of the Hα profile observed on the night of HJD 2,458,538 and the determined bisector location. The RV measurements made from the He I profiles have too much scatter to improve upon the Hα RV curve. Thus, we restricted the orbital solution to the Hα measurements only, and we report the long-term corrected results in Table 2.

We collected seven FUV measurements of the sdO RVs (four IUE and three HST) to determine a preliminary double-lined orbital solution. We tried both circular and elliptical fits to the RV measurements and found that the elliptical solution offered no significant improvement. Table 6 lists both the single-lined (Be) and double-lined (Be+sdO) fitting results, and the double-lined solutions are shown in Figure 8.

We also measured relative RVs for the Hβ line in the same way as for HD 152478. These were also corrected for long-term trends. These measurements (given in Table B2) are shown as a function of the double-lined fit orbital phase in panel (b) of Figure B3 in Appendix B. The Hβ RV curve is similar to the Hα case but displays more scatter.

Table 6
Circular Orbital Elements of HD 157042

Element	Value	
	SB1	SB2
P (days)	178.64 ± 0.12	176.17 ± 0.04
T_{sc} (HJD−2,400,000)	58,650.3 ± 0.4	58,654.2 ± 0.5
K_1 (km s^{-1})	6.08 ± 0.03	5.80 ± 0.06
K_2 (km s^{-1})	…	57.6 ± 0.6
q	…	0.101 ± 0.001
γ_1 (km s^{-1})	2.24 ± 0.05	2.38 ± 0.06
γ_2 (km s^{-1})	…	−10.2 ± 0.8
$f(m_1)$ ($\mathcal{M}_\odot^N$)	0.0042 ± 0.0001	0.0033 ± 0.0001
$f(m_2)$ ($\mathcal{M}_\odot^N$)	…	3.50 ± 0.10
$a_1 \sin i$ ($\mathcal{R}_\odot^N$)	21.44 ± 0.12	19.61 ± 0.21
$a_2 \sin i$ ($\mathcal{R}_\odot^N$)	…	200.7 ± 1.9
$a \sin i$ ($\mathcal{R}_\odot^N$)	…	220 ± 3
$M_1 \sin^3 i$ ($\mathcal{M}_\odot^N$)	…	3.88 ± 0.21
$M_2 \sin^3 i$ ($\mathcal{M}_\odot^N$)	…	0.426 ± 0.024
rms$_1$ (km s^{-1})	2.9	2.9
rms$_2$ (km s^{-1})	…	4.0

3.5. HD 157832

The spectra of HD 157832 show strong Hα and Hβ emission line profiles. We observed weak double-peaked emission features in He I $\lambda\lambda$4921, 5015, while He I λ5875 appears as a broad weak absorption line. Metallic emission profiles occur in Fe II $\lambda\lambda$4583, 5020, 5169, 5197, 5234, 5276, 5284, 5316,

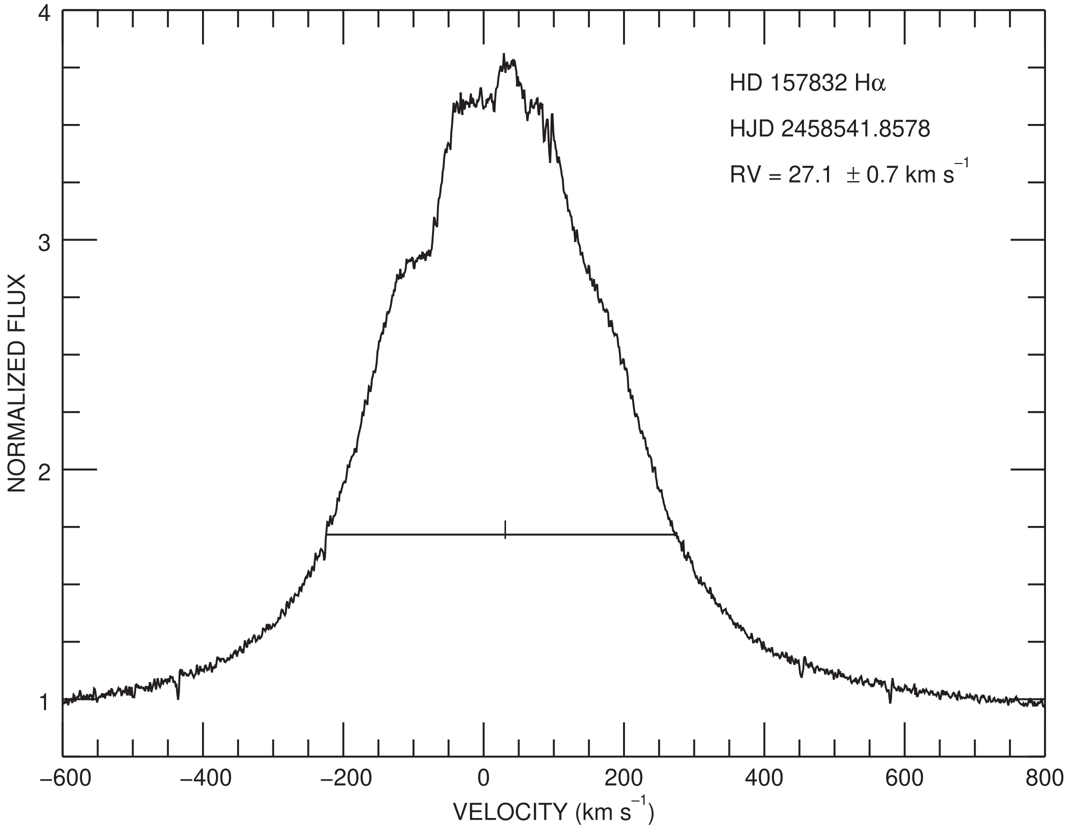

Figure 9. The Hα profile of HD 157832 observed on the night of HJD 2,458,541. The RV measured from the broad wings using the bisector technique is shown as the tick mark.

Table 7
Circular Orbital Elements of HD 157832

Element	Value
P (days)	95.23 ± 0.07
$T_{\rm sc}$ (HJD−2,400,000)	58,566.3 ± 0.4
K_1 (km s^{-1})	6.25 ± 0.20
γ (km s^{-1})	18.85 ± 0.10
$f(m)$ ($\mathcal{M}_\odot^{\rm N}$)	0.0024 ± 0.0002
$a_1 \sin i$ ($\mathcal{R}_\odot^{\rm N}$)	11.76 ± 0.37
rms (km s^{-1})	1.0

Table 8
Companion Star Mass for HD 157832

Inclination (deg)	q (M_2/M_1)	M_2 ($\mathcal{M}_\odot^{\rm N}$)
60	0.073	0.80
65	0.070	0.77
70	0.067	0.74
75	0.065	0.72
80	0.064	0.70

5362, 6148, 6383, 6385, 6456, 7516, 8451, N II λ4630, N II or Fe II λ5535, Si II $\lambda\lambda$6239, 6347, 6371, Al II λ6243, O I $\lambda\lambda$7771, 7774, 7775, 8446, and Ca II $\lambda\lambda$8542, 8600 (Ca II $\lambda\lambda$8498, 8662 were positioned too close to the echelle order boundaries). Doppler shifts of Hα and Hβ were measured from the broad emission wings, and the RVs were corrected for the systematic shifts reported in Appendix A. Figure 9 shows an example of the Hα profile observed on the night of HJD 2,458,541 with the marked position of the measured bisector wing velocity. We report the corrected Doppler shifts and their associated errors from the Hα profiles in Table 2.

Additional relative RV measurements were made using the CCF approach to measure the CCF peak RVs for weak emission line features observed in He I, Fe II $\lambda\lambda$5197, 5234, 5276, 5284, and O I λ8446. For the Fe II λ6456 and Ca II $\lambda\lambda$8542, 8600 profiles, the Doppler shifts were determined from the broad CCF wings. The RV curves of these lines were plotted from the ephemeris reported in Table 7 and are shown in Figure B4 of Appendix B. The RV measurements are similar to those of Hα but display more scatter. These measurements are included in Table B3 of Appendix B.

Wang et al. (2018) reported the detection of a weak signal of the sdO companion star based upon two FUV spectra from IUE. However, later HST FUV spectroscopy did not confirm this detection (Wang et al. 2021). Thus, we restricted the fit to the Be star RV measurements to obtain a single-lined orbital solution of this binary system from a circular orbital fit of the corrected velocities, and the elements are given in Table 7. The epoch $T_{\rm SC}$ refers to the time of Be star superior conjunction. Seven RV measurements observed between the nights of HJD 2,458,635 and HJD 2,458,667 were assigned zero weight for the orbital fit. These spectra displayed large deviations from the fit and showed a steep drop in intensity in the blue wings of Hα (see Figure B1 of Appendix B). Figure 10 shows the orbital velocities and the derived fit. Additional RV plots with more scatter are given for Hβ

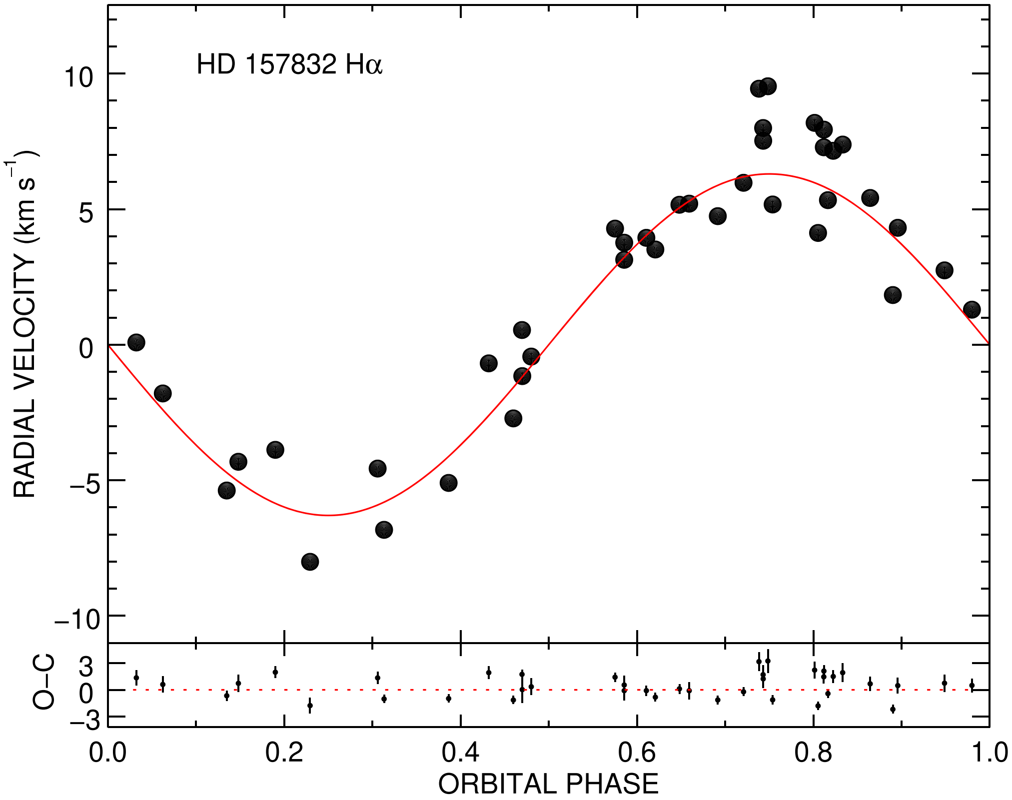

Figure 10. Relative RV curve (red) for the Be star HD 157832 from the Hα measurements (black) shown in the same format as Figure 2.

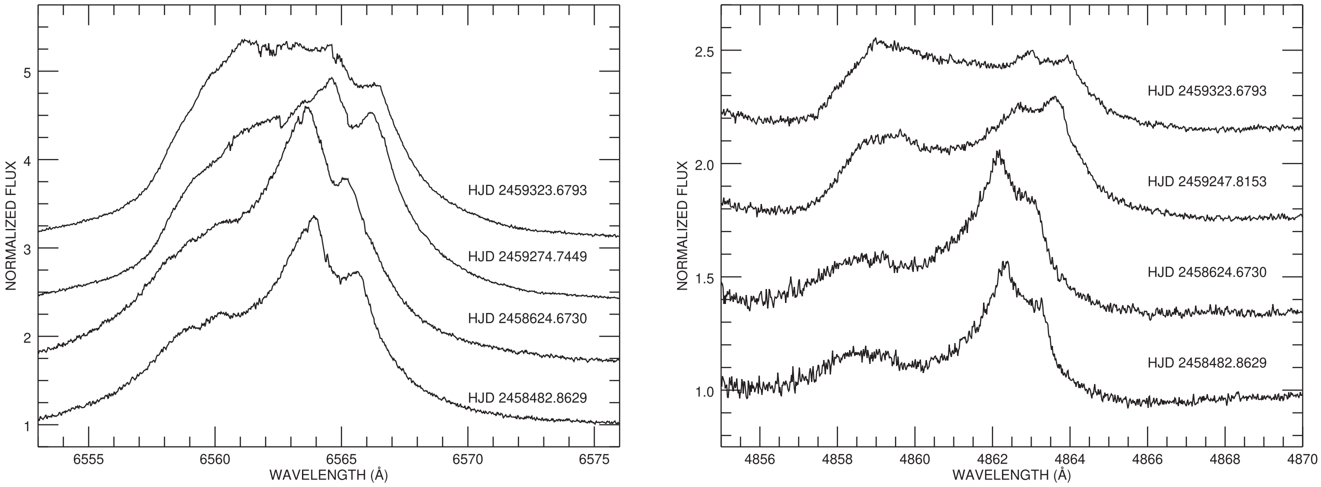

(a) Hα

(b) Hβ

Figure 11. Emission profile variations of HD 113120 for Hα (left) and Hβ (right). This subsample is arranged with vertical offsets that increase with time.

in panel (c) of Figure B3 and for He I λ5015 and Fe II λ5020, Fe II $\lambda\lambda$5197, 5234, 5276, O I λ8446, and Ca II $\lambda\lambda$8542, 8600 in Figure B4 of Appendix B.

We can use the orbital mass function and an estimate of the Be star mass to find a mass range for the companion. Lopes de Oliveira & Motch (2011) determined $T_{\rm eff} = 25{,}000 \pm 1000$ K from a spectral energy distribution (SED) fit, and Be stars with similar temperatures in the list compiled by Zorec et al. (2016) have a mass of about 11 $\mathcal{M}_{\odot}^{\rm N}$. Table 8 shows the estimated masses of the companion for several values of orbital inclination.

4. Spectral Variability of the Be Stars

The observed Balmer profiles and metallic lines display spectral variations in the target stars. Here we document the line variability appearing in the spectra and measure their equivalent width values (W_λ) by adopting the convention of positive W_λ values for stellar absorption profiles and negative values for emission lines.

4.1. HD 113120

The emission profiles of Hα and Hβ displayed striking variations in shape through the observing campaign. Figure 11

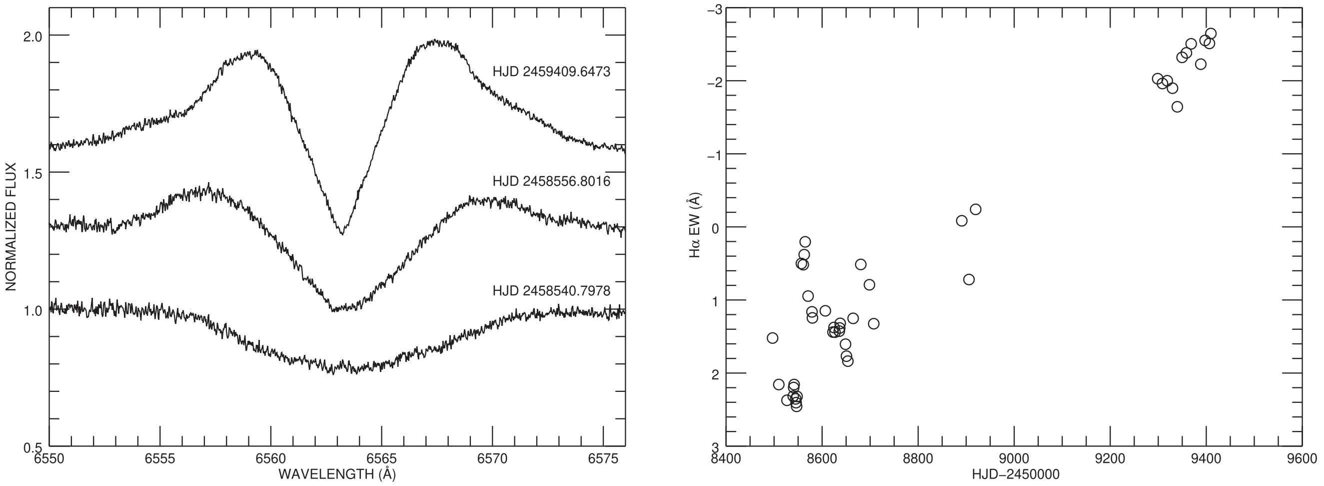

(a) Hα (b) $W_{\mathrm{H}\alpha}$

Figure 12. The Hα variations of HD 137387. Panel (a) shows the growth of new emission on short and long timescales with offsets of +0.3 and +0.6 in normalized flux. Panel (b) shows the time evolution of the equivalent width W_λ (summed over the wavelength range from 6552 to 6578 Å).

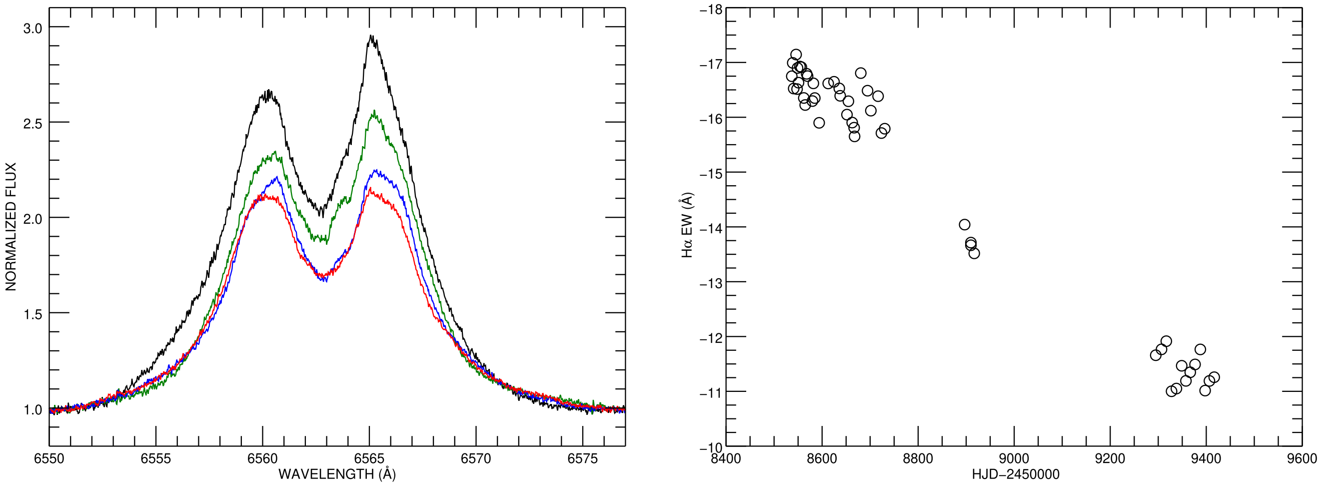

(a) Hα (b) $W_{\mathrm{H}\alpha}$

Figure 13. (a) Hα variations of HD 152478. The red peak dominated at the beginning of the observing campaign (black; HJD 2,458,536). The profile gradually decreased in strength (green, HJD 2,458,916; blue, HJD 2,459,294). The red and violet emission peaks reached a comparable and lower strength toward the end of the observations (red; HJD 2,459,416). (b) Temporal evolution of the Hα equivalent width (integrated over 6552–6577 Å).

shows a subset of the profiles to illustrate the changes on several timescales. At the beginning of the observing sequence (HJD 2,458,482), the profiles are marked by a strong central peak plus subpeaks in the red and far blue. After 142 days, the central peak increased in strength but was almost absent some 650 days later, while the red and blue peaks continued to grow. In the final spectrum (HJD 2,459,323), the central region appears as a plateau. The basic variations seen in Hα are also present in Hβ, but the latter is more influenced by the changes in the subpeaks. These subpeaks also appear as a narrow emission component in the He I λ6678 line.

We measured the W_λ values of the Hα, Hβ, and He I λλ6678, 7065 profiles, and these are collected in Table C2 of Appendix C. Time plots of the measured W_λ values are given in Figure C1. All four lines show a rapid increase in emission over the first 100 days of observation. Slower increases followed for Hα and Hβ, while the He I emission generally declined. These changes are consistent with an episode of increased mass ejection into the base of the disk followed by an outward expansion of a density enhancement.

4.2. HD 137387

The spectra of HD 137387 showed broad absorption in the Hβ, He I, and metallic lines. However, in the case of Hα, the profile changed from broad absorption (see the spectrum observed on HJD 2,458,540 in Figure 12) to a narrower shell absorption profile superimposed upon broad emission (see HJD 2,459,409). The associated change in the Hα equivalent width is shown in panel (b) of Figure 12. The W_λ measurements of Hα, Hβ, He I λλ4921, 5015, 5875, 6678, 7065, and Ca II λ8542 are given in Table C2 of Appendix C. The temporal variations of these W_λ measurements are shown in Figure C2.

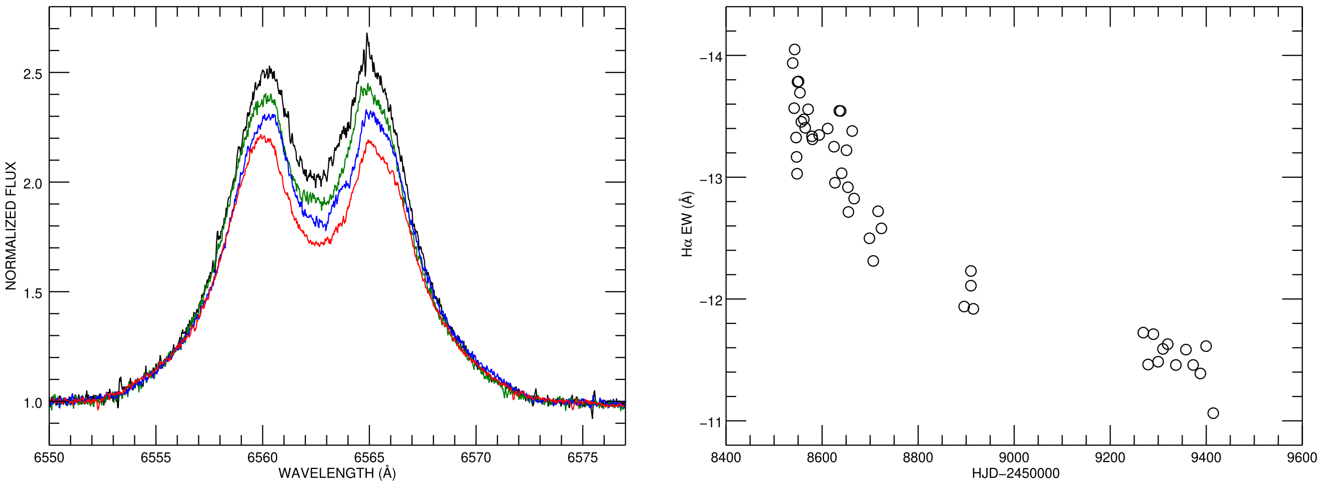

(a) Hα (b) $W_{\text{H}\alpha}$

Figure 14. (a) The Hα profiles of HD 157042 displayed a gradual weakening throughout the observing campaign. Observations made on the nights of HJD 2,458,538, 2,458,716, 2,458,909, and 2,459,414 are plotted in black, green, blue, and red, respectively. (b) Temporal variations of the Hα equivalent width (integrated over the range 6551–6574 Å).

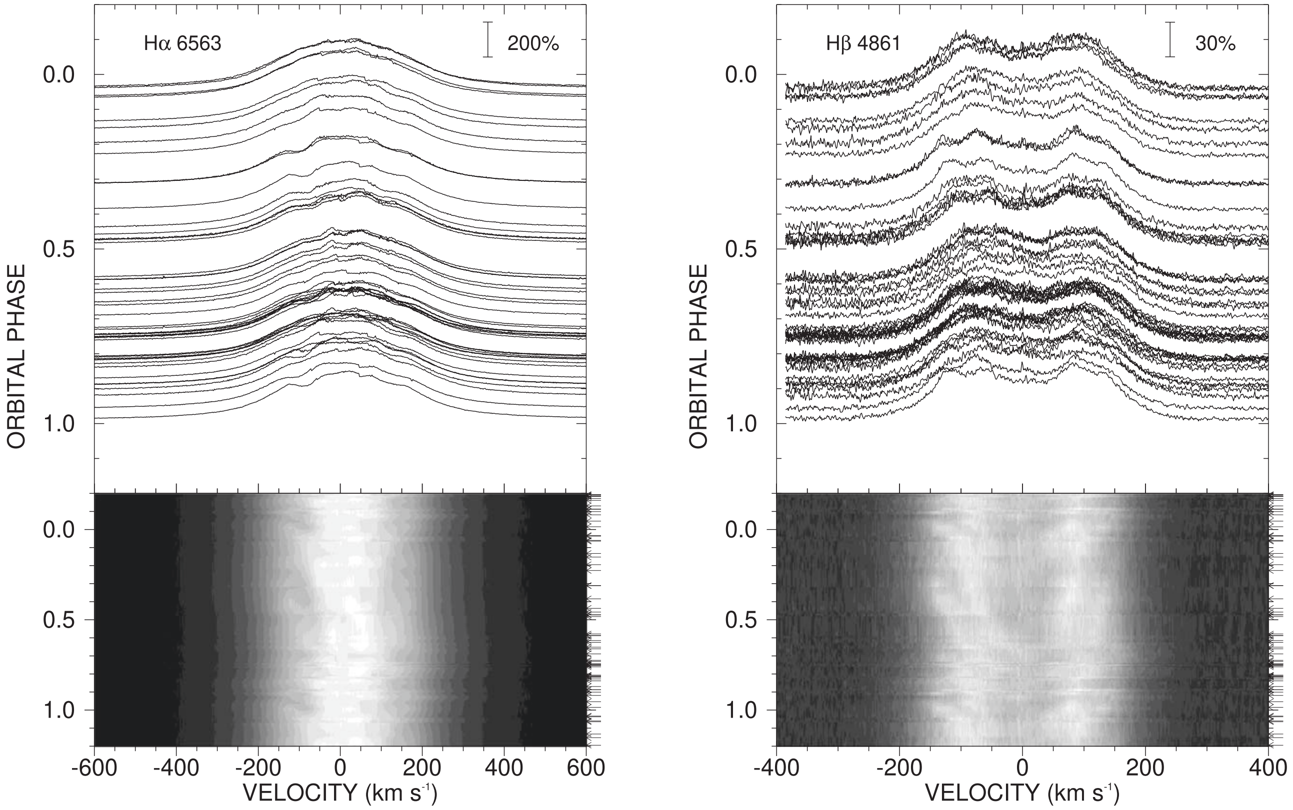

Figure 15. Left: Hα profiles of HD 157832 plotted as a function of the orbital phase and Doppler shift. The continuum of each profile is aligned with the orbital phase in the top panel, and the flux scale relative to the continuum is indicated by the vertical bar in the upper right corner. A gray-scale version of the profiles appears in the bottom panel, in which the brightness scales with emission flux above the continuum. The arrows indicating the orbital phases of the observations are marked along the right ordinate. Right: Hβ profiles plotted in the same format as the left panel but for different flux scaling.

4.3. HD 152478

The double-peaked emission features of Hα for HD 152478 displayed a change in V/R. At the beginning of the observing campaign, the profile had a red peak that was stronger than the violet peak (HJD 2,458,536; black in panel (a) of Figure 13). The asymmetry in the peak strength diminished over 380 days (HJD 2,458,916; green), and the two emission peaks attained comparable strength by HJD 2,459,294 (blue). The overall emission strength decreased to a minimum at the end of the campaign (HJD 2,459,416; red). The time evolution of the Hα equivalent width is shown in panel (b) of Figure 13. The W_λ measurements are collected in Table C2 of Appendix C, together with measurements of Hβ and He I λλ4921, 6678, 7065.

4.4. HD 157042

The V and R peaks of the Hα emission profiles of HD 157042 displayed comparable relative strength over the time span of the observations. However, the whole profile showed a gradual decrease in strength over time (see panel (a) of Figure 14). No significant spectral variations appeared in the Hβ, He I, and metallic line profiles. We report the measured W_λ values of Hα, Hβ, and He I $\lambda\lambda$4921, 6678, 7065 in Table C2 of Appendix C.

4.5. HD 157832

The Hα emission profiles of HD 157832 are broad and strong, and they are marked by narrower subfeatures that appear to vary with orbital phase. The Hα and Hβ profiles are plotted as functions of Doppler shift and orbital phase in Figure 15. The top panels show the profiles offset according to orbital phase, while the bottom panels portray the emission flux as a gray-scale image. These show that the profiles exhibit migrating subfeatures. For example, a weak depression appears in the blue wing of Hα near $V_r = -75$ km s^{-1} at $\phi = 0.3$, and this subfeature moves slightly redward to persist for a part of the orbit. The subfeatures are more striking in Hβ, and excess emission appears in subfeatures at orbital phases $\phi = 0.0$ and 0.5 that progress from both line wings toward the line center (right panel of Figure 15). We give the W_λ measurements for Hα and Hβ in Table C2 of Appendix C. The appearance of coherent patterns of emission in spectra from many different orbital cycles offers independent support for the period derived from the RVs (Section 3.5).

Such phase-locked spectral variability appears in the Balmer profiles of other Be binaries. For example, the variations of the Hβ profiles of HD 157832 are very similar to those observed in HD 55606 by Chojnowski et al. (2018; see the bottom panels of their Figure 7). Chojnowski et al. (2018) argued that the variations are related to a two-armed spiral density pattern in the Be star disk that results from the tidal pull of the companion (see the models of Panoglou et al. 2018). The portion of a spiral arm that is aligned with the line of sight will concentrate emission flux at a Doppler shift associated with the Keplerian velocity at the distance of the arm from the Be star. We first observe the excess flux from the inner part of the arm at high speed, and then we sample the line-of-sight portions of the arm at larger radii and lower speed as the orbit progresses. This is observed as an emission subfeature that is first seen in the line wing and then progresses toward the line center. In a two-armed spiral, this occurs twice each orbit with the motions of one arm mirrored in velocity space by the other arm.

5. Secondary Lines in the Visual Spectrum

The spectral signature of the hot sdO companions of the targets were discovered in the ultraviolet, where a host of narrow absorption lines are detected through cross-correlation analysis (Wang et al. 2021). We made a visual inspection for similar narrow-lined features in the visible spectra recorded by CHIRON, but none were found. This is not surprising given the expected faintness of the sdO spectrum in the visible region (see below). Thus, direct measurements of the RVs of the hot companions are still limited to those from ultraviolet spectroscopy from IUE and HST that we used in the previous section for preliminary double-lined orbital solutions.

Nevertheless, we can predict the spectral appearance of the sdO stars in the visible band using the stellar parameters and flux ratio determined from the analysis of the ultraviolet spectrum. Here we focus on the spectral region in the immediate vicinity of the He II λ4686 transition. This feature is prominent in all hot, O-type spectra and absent in the cooler B-type spectra of the Be star components. Indeed, the first discovery of a Be+sdO binary was made thanks to the presence of He II λ4686 in the spectrum of ϕ Per (Poeckert 1981).

Our goal in this section is to compare the predicted visible spectrum of the sdO component with the CHIRON spectroscopy. We used the TLUSTY solar-metallicity atmosphere models from Lanz & Hubeny (2003, 2007) to create model spectra for the hotter sdO and cooler Be components, respectively. The first step was to estimate the monochromatic flux ratio of the stars f_2/f_1 in the vicinity of the He II λ4686 line. We adopted the stellar parameters (effective temperature, gravity) of the Be stars from Wang et al. (2021) to create model SEDs. The SEDs for the sdO stars were set according to the temperatures derived by Wang et al. (2021) with the gravity set to $\log g = 4.75$, the largest value available in the TLUSTY grid but probably lower than the actual gravities. We formed the ratio of the sdO-to-Be fluxes by normalizing the ratio to the derived value in the 1450–1460 Å region (Wang et al. 2021). We then evaluated the wavelength-dependent flux ratio f_2/f_1 in the continuum adjacent to He II λ4686. The expected sdO flux contributions are low: $f_2/f_1 = 0.018$, 0.018, 0.017, and 0.019 for HD 113120, HD 137387, HD 152478, and HD 157042, respectively (there was no detection and hence no flux ratio estimate for HD 157832). Finally, the detailed spectrum of the sdO star was derived from the TLUSTY models for the same wavelength grid as that of the CHIRON echelle order recording He II λ4686, and this model spectrum was normalized to its expected net flux contribution, $f_2/(f_1 + f_2)$.

We used a Doppler tomography algorithm (Bagnuolo et al. 1994) with the preliminary orbital velocity solutions to reconstruct the individual spectral components of the Be and sdO stars from the entire set of CHIRON spectra for each target. The reconstructed spectra have a much higher signal-to-noise ratio (S/N) than the individual spectra. The distribution of flux between components is set in advance, and we arbitrarily assigned the sdO fluxes to the predicted values extrapolated from the ultraviolet flux ratios. The final results are plotted in Figure 16 in units of the combined flux $f_2/(f_1 + f_2)$. The solid lines depict the reconstructed sdO spectra that were smoothed to a resolving power of $R = 8800$ to improve the spectral S/N. These are compared to the predicted model spectra (also smoothed), shown as dotted lines. We see that the He II λ4686 absorption line is present and appears similar to the model predictions in all of the sdO spectra except for the case of HD 157832, where no He II line is detected. The reconstructed spectrum of the secondary of HD 157832 shown in Figure 16 was obtained using Doppler shifts based upon a trial mass ratio of $M_2/M_1 = 0.1$, but we arrived at similar nondetections of He II λ4686 using a range of mass ratios (0.05–0.13) for the reconstruction. This is consistent with the lack of detection of the sdO lines in the ultraviolet spectrum of HD 157832 from HST (Wang et al. 2021). This suggests that the companion of HD 157832 is either too cool to create a He II line or much fainter than that found in the other cases. The velocity registration of the observed and model profiles is generally good except in the case of HD 137387, which

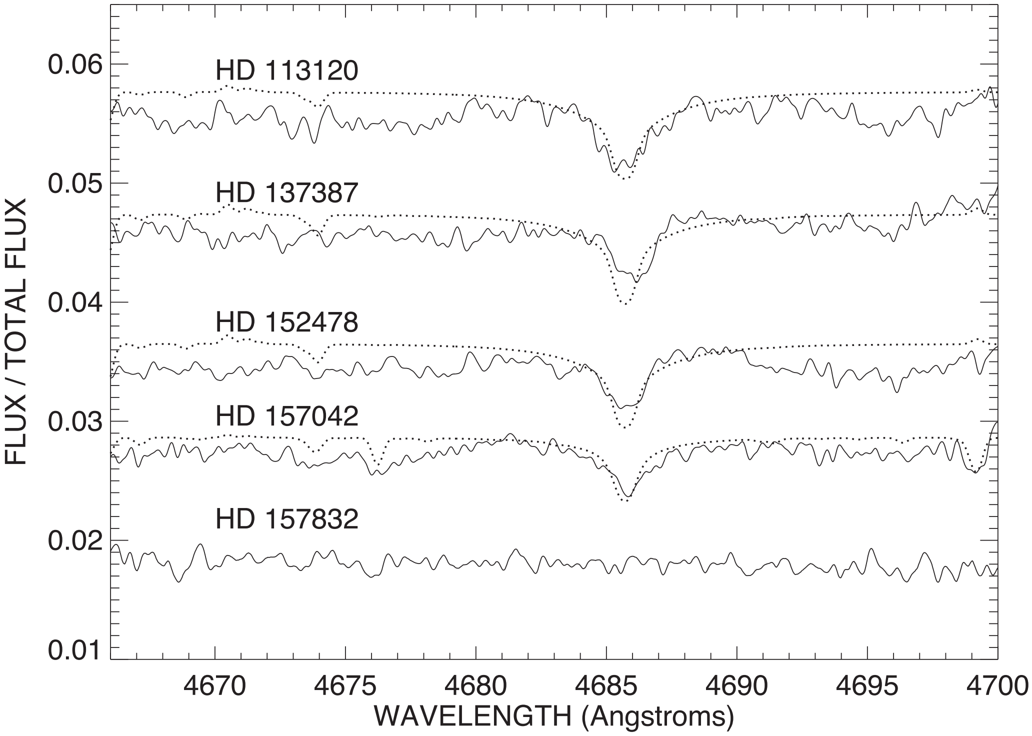

Figure 16. Spectra of the sdO components from Doppler tomography reconstructions of the CHIRON spectroscopy (solid lines) that were made using the preliminary double-lined orbital velocity solutions. There is no double-lined orbit for HD 157832, so we assumed a reflex motion of the companion for a mass ratio of $M_2/M_1 = 0.1$ and then plotted the reconstructed spectrum for a supposed flux contribution of $f_2/(f_1 + f_2) = 0.018$. The TLUSTY model spectra predicted from analysis of the HST ultraviolet spectra (Wang et al. 2021) are overplotted as dotted lines. The reconstructed and model spectra are shown with vertical offsets of 0.04, 0.03, 0.02, and 0.01 for HD 113120, HD 137387, HD 152478, and HD 157042, respectively, for ease of comparison. The reconstructed spectra reveal the presence of the expected He II λ4686 line in all but the case of HD 157832.

suggests that the systemic velocity derived from the preliminary double-lined orbit may need adjustment for the He II λ4686 line.

The presence of the He II λ4686 line in the reconstructed spectra of the faint companions confirms that the spectral signal of the sdO stars is found in the visible spectrum. However, their flux contribution in the visible is small, and it would require very high S/N spectroscopy to detect the He II λ4686 line in an individual spectrum. The success of the tomographic reconstructions in finding such faint features attests to the reliability of our preliminary orbital solutions that were the basis of the tomographic reconstructions.

6. Discussion

Since the first detection of the stripped helium star in the ϕ Per binary system, multiwavelength search efforts using optical and FUV spectroscopy and near-IR ground-based interferometry have led to the detection and characterization of the orbital and physical properties of eight confirmed Be+sdO binaries. Our work has provided preliminary double-lined orbits for four additional systems, so it is worthwhile to review the orbital and physical properties of the current sample. We list in Table 9 our results for these double-lined systems plus HD 157832. We give estimates of the Be star mass in Table 9 from prior work by Tetzlaff et al. (2011) and Zorec et al. (2016). The values of $M_{\rm Be}$ shown are the means of the estimates from these two works with uncertainties that span the ranges from both. Unfortunately, there are no prior estimates for the mass of HD 157832, so we simply list an estimate from Be stars of a similar effective temperature (Lopes de Oliveira & Motch 2011) in the compilation by Zorec et al. (2016). Then the masses of the companions $M_{\rm sdO}$ follow from the mass ratios quoted in the orbital solutions given in Section 3 (or from Table 8 in the case of HD 157832).

Table 9 also collects results on the orbital period, Be star semiamplitude K_1, and stellar masses of the other confirmed Be+sdO binaries, candidate systems, and recent detections of Be binaries among the γ Cas analog stars with hard X-ray emission (Nazé et al. 2022). The periods and masses of the systems discussed here are similar to those of the other confirmed binaries. There are now three systems, HD 113120, HD 137387, and HD 194335, that have sdO masses above the Chandrasekhar limit, and these are potentially the progenitors of hydrogen-poor SNe that will leave a neutron star remnant in a Be X-ray binary (BeXRB).

The periods of the five systems discussed here tend to be longer than those from prior investigations. For example, HD 152478 has the longest orbital period of 237 days in the known population. We suspect that this is a selection effect. Determinations of the earlier binary solutions were more favorable in shorter-period systems where the Be star semiamplitudes K_1 are larger. On the other hand, our sample was selected from detections of the sdO FUV spectrum in a larger survey of the ultraviolet spectra (Wang et al. 2018), so the longer periods in the current sample are probably more representative of Be+sdO binaries as a whole.

We now have a sample of 12 systems (eight prior plus four new) with known mass ratios, and the mean ratio is $q = M_2/M_1 = 0.124 \pm 0.059$ or $Q = M_1/M_2 = 8.1 \pm 3.8$, where the error is the standard deviation of the sample. The scatter in q between systems is larger than the individual

Table 9
Be+sdO Binary Systems with Orbital Periods

HD Number	Star Name	Orbital Period (days)	K_1 (km s^{-1})	$M_{\rm Be}$ ($\mathcal{M}_\odot^{\rm N}$)	$M_{\rm sdO}$ ($\mathcal{M}_\odot^{\rm N}$)	References
This Work						
113120	LS Mus	181.54 ± 0.11	10.66 ± 0.03	10.1 ± 2.2	1.43 ± 0.31	…
137387	κ Aps	192.1 ± 0.1	9.09 ± 0.08	11.8 ± 1.0	1.60 ± 0.14	…
152478	V846 Ara	236.50 ± 0.18	4.33 ± 0.05	6.5 ± 1.3	0.53 ± 0.11	…
157042	ι Ara	176.17 ± 0.04	5.80 ± 0.06	10.5 ± 2.9	1.06 ± 0.29	…
157832	V750 Ara	95.23 ± 0.07	6.25 ± 0.20	11[a]	0.7[b]	…
FUV Confirmed Be+sdO Binary Systems						
10516	ϕ Per	126.6982 ± 0.0035	10.2 ± 1.0	9.6 ± 0.3	1.2 ± 0.2	Mourard et al. (2015)
41335	HR 2142	80.913 ± 0.018	7.1 ± 0.5	9	0.7	Peters et al. (2016)
55606	BD−01 1603	93.76 ± 0.02	10.74 ± 1.17	6.0−6.6	0.83−0.90	Chojnowski et al. (2018)
58978	FY CMa	37.253 ± 0.007	17.4 ± 0.9	10−13	1.1−1.5	Peters et al. (2008)
109387	κ Dra	61.5496 ± 0.0058	6.90 ± 0.15	3.65 ± 0.48	0.426 ± 0.043	Klement et al. (2022a)
194335	V2119 Cyg	63.146 ± 0.003	…	8.65 ± 0.35	1.62 ± 0.28	Klement et al. (2022b)
200120	59 Cyg	28.1871 ± 0.0011	11.7 ± 0.9	6.3−9.4	0.62−0.91	Peters et al. (2013)
200310	60 Cyg	147.68 ± 0.03	11.6 ± 1.2	7.3 ± 1.1	1.2 ± 0.2	Klement et al. (2022b)
Be+sdO/sdB Binary Candidates Identified from Optical Spectroscopy						
37202	ζ Tau	132.987 ± 0.050	7.43 ± 0.46	11	0.87−1.02	Ruždjak et al. (2009)
63462	o Pup	28.903 ± 0.004	10.3 ± 9.6	11−15	0.7 ± 1.0	Koubský et al. (2012)
68980	MX Pup	5.1526 ± 0.0011	0.90	15	0.6−6.6	Carrier et al. (2002)
148184	χ Oph	138.8 ± 1.3	15.0 ± 1.8	10	1.7−2.0	Abt & Levy (1978)
161306	MWC 271	99.90 ± 0.50	4.90 ± 1.53	15	0.9	Koubský et al. (2014)
167128	HR 6819	40.334 ± 0.005	3.9 ± 0.7	6	0.4−0.8	Gies & Wang (2020)
183537	7 Vul	69.4212 ± 0.0034	8.86 ± 0.62	5.47−8.98	0.56−0.91	Harmanec et al. (2020)
184279	V1294 Aql	192.91 ± 0.18	6.26 ± 0.61	16.9	1.171−1.361	Harmanec et al. (2022)
…	LB−1	78.7999 ± 0.0097	11.2 ± 1.0	7 ± 2	1.5 ± 0.4	Shenar et al. (2020)
γ Cas Analog Be Binaries[b]						
5394	γ Cas	203.52 ± 0.08	4.297 ± 0.090	13	0.98	Nemravová et al. (2012)
12882	V782 Cas	122.0 ± 1.5	5.2 ± 0.9	9	0.6−0.7	Nazé et al. (2022)
45995	BD+11 1204	103.1 ± 1.0	6.7 ± 0.4	10	1.0 ± 0.1	Nazé et al. (2022)
183362	V558 Lyr	83.3 ± 1.8	8.2 ± 1.1	8	0.7−0.8	Nazé et al. (2022)
212571	π Aqr	84.07 ± 0.02	16.7 ± 0.2	15 ± 3	2.4 ± 0.5	Bjorkman et al. (2002)
220058	V810 Cas	75.8 ± 0.7	6.4 ± 0.7	12.5	0.7−0.8	Nazé et al. (2022)
…	SAO 49725	26.11 ± 0.08	2.8 ± 0.5	13	0.2−0.5	Nazé et al. (2022)
…	V2156 Cyg	126.6 ± 2.0	5.5 ± 0.7	11	0.7−0.8	Nazé et al. (2022)

Notes.
[a] Based upon mass estimates for Be stars of similar effective temperature.
[b] Companion may not be sdO type.

Table 10
Orbital and Rotational Inclinations

HD Number	i (Orbital) (deg)	i (Rotational) (deg)
113120	74 ± 4	63 ± 15
137387	60 ± 4	50 ± 12
152478	60 ± 7	60 ± 15
157042	46 ± 6	59 ± 14

uncertainties, so there are significant differences in mass ratio among the systems. However, there is no apparent dependence of mass ratio on the Be star mass. Thus, if the mass ratio after stripping of the envelope of the donor is independent of mass, then we may expect that sdO remnants with masses greater than the Chandrasekhar limit will generally be found in binaries with Be star masses greater than 8.1 × 1.4 = 11.3 $M_\odot$. This is consistent with the finding that the descendants of the massive Be+sdO systems, the BeXRBs, have Be star masses that are never less than 8 $M_\odot$ (Reig 2011).

It is useful to compare estimates of the orbital inclination with those for the Be star and its disk because on evolutionary grounds, we expect that mass transfer transformed orbital angular momentum into spin angular momentum. Future interferometric observations should yield the orbital (and possibly disk) inclination (Klement et al. 2022a, 2022b). However, we can estimate the orbital inclination from the $M_1 \sin^3 i$ products given in Section 3 and the estimated masses of the Be star given in Table 9. These orbital inclination estimates are given in the second column of Table 10 for the four systems with double-lined orbital solutions. The orbital inclination values generally agree within the errors with the stellar rotational inclinations derived by Zorec et al. (2016;

third column). Thus, the inclination estimates for these four systems agree with predictions that the orbital and Be star spin inclinations are the same.

Shao & Li (2014) performed theoretical calculations to simulate the population of Be binary systems in the local Galactic environment using a BPS code. The authors investigated the population distribution considering both stable mass transfer and a common envelope channel during the early stage of the binary interaction. They concluded that Be binaries with helium star companions are likely formed through stable mass transfer, and they avoid a spiral-in associated with the common envelope phase. A tailored BPS calculation was conducted by Shao & Li (2021) to predict the population distribution of Galactic Be+He binaries and compare the results with observational data on confirmed Be+sdO binaries determined from FUV spectroscopy and the recently proposed Be+He binaries of LB−1 (Shenar et al. 2020) and HR 6819 (Gies & Wang 2020). The simulations map the parameter space (including [$M_{\rm He}$, $M_{\rm Be}$] and [$P_{\rm orb}$, $M_{\rm Be}$]) for the Be binary systems that have evolved through either Case A or Case B scenarios[6] and include several cases of mass transfer efficiency. They conclude that Case B mass transfer is likely responsible for forming most of the population of Be+He binaries. Furthermore, models that assume almost conservative mass transfer (i.e., no systemic mass loss) yield mass ratios after stripping that agree with the observations (see their Figure 1, lower right panel).

It is difficult at present to compare the model and observed distributions of mass and orbital period because the sample is small and subject to selection effects. Shao & Li (2021) found that most of the post–mass transfer binaries have a mass distribution that attains a maximum around ∼3–5 $\mathcal{M}_\odot^{\rm N}$ for the Be star and ∼0.3–0.6 $\mathcal{M}_\odot^{\rm N}$ for the He star. These are lower than found among the known systems, with the exception of the case of κ Dra that has lower masses and cooler temperatures than the rest (Klement et al. 2022b). The model orbital period distribution peaks over the range of 25−100 days, and this is significantly lower than the 95–237 day range of the new sample.

The current models may need further development to capture all of the important processes. For example, Be stars may have experienced rotation-dependent mass accretion during their early accretion history (Stancliffe & Eldridge 2009). In addition, recent theoretical studies suggest that giant donor stars may enable stable mass transfer and avoid a common envelope stage. Ge et al. (2020) utilized an adiabatic mass-loss model to simulate the evolutionary state of binary stars, in which the donor stars reach the red giant branch (RGB) and asymptotic giant branch (AGB). They concluded that these binaries may significantly expand the parameter space of systems that undergo stable mass transfer than those previously suggested by the BPS calculations. A similar result is obtained by Temmink et al. (2022) from 1D MESA simulations of the mass transfer stability for a wide range of interacting binaries. These findings open up the possibility of the formation of the Be+sdO systems through interactions with a more evolved giant donor star. Future improvements in the simulations, such as careful treatments of stellar winds, tidal interactions, and stellar rotation in the mass transfer and accretion histories, may be needed to reproduce the observed sample.

7. Conclusions

Growing evidence suggests that the rapid rotation of Be stars is likely a consequence of past mass and angular momentum accretion from a companion star. If so, many Be stars will have hot helium star companions that are the stripped remnants of the donor stars. Searches for the signature of the stripped helium companion stars are best accomplished in the FUV region of the spectra, and a number of prior studies have utilized IUE and HST FUV spectroscopy to detect the spectral signatures and properties of the stripped helium stars. However, two of the most important evolutionary pillars, the orbital period and the stellar mass of the helium star, are still missing in many cases. In this work, we have carried out a 3 yr observing campaign of high-S/N and high resolving power spectroscopy to determine these missing quantities for five Be +sdO binary systems visible in the southern sky. The Be star spectra have lines that are much broader than the orbital Doppler shifts and often blended with emission components from the disks, so the Doppler shift measurements are difficult, and orbital solutions require long sequences of observations. Based upon a careful spectral line inspection, we succeeded in measuring the Doppler shifts of the Be stars, and, combining these with velocities for the sdO components from prior FUV spectroscopy, we determined the orbital solutions of these binary systems.

The binaries in our sample have long orbital periods (P from 95 to 237 days) with small Be star semiamplitudes ($K_1 < 11$ km s^{-1}). Using the derived semiamplitude ratios and independent estimates of Be star mass, we determined preliminary mass estimates of the subdwarf companion stars. The sdO stars have estimated masses in the range from 0.5 to 1.7 $\mathcal{M}_\odot^{\rm N}$, which is consistent with the masses reported in other Be+sdO binaries from prior investigations. The stripped helium stars in HD 113120 and HD 137387 have estimated masses greater than the Chandrasekhar mass limit of 1.4 $M_\odot$, indicating that the sdO stars in these systems may be progenitors of SNe Ib and Ic. We also documented the line variations appearing in the spectra on orbital and nonorbital timescales. One of the stars, HD 157832, displays phase-locked subfeatures that appear in the Hα and Hβ emission profiles. Such features may result from a two-armed spiral density wave pattern in the circumstellar disk that is due to the tidal pull of the companion star.

We also made a search for spectral features of the faint sdO stars by making a Doppler tomography reconstruction of the component spectra using the new orbital solutions. The reconstructed spectra of the secondary show the presence of a He II λ4686 absorption line in four of the targets with a strength consistent with model predictions for the sdO stars from the analysis of their FUV spectra. This confirms the presence of a hot stripped companion in these cases. However, the He II line is absent from the reconstructed secondary spectrum in the case of HD 157832, indicating that any hot companion must be very faint. This agrees with the lack of a hot spectral signature in the FUV spectra of this star from HST (Wang et al. 2021), and it casts doubt on the marginal detection of the sdO signal in the IUE spectrum (Wang et al. 2018).

---

[6] Case A mass transfer refers to an interacting binary system in which the donor is a main-sequence star in the core hydrogen-burning phase when it fills its Roche lobe. In Case B, mass transfer occurs when the donor is in or evolving to the red giant phase with hydrogen shell burning following core exhaustion. Case C refers to the case when the donor is in an advanced phase after helium core exhaustion.

Theoretical simulations by Shao & Li (2021) and others predict that the population of Be+He binaries should be abundant but often hidden from detection in the local Galactic environment. These binaries likely experienced stable mass transfer during their earlier Case B interaction, and models that assume conservative mass transfer provide the best match to the observed ratios of the He-to-Be star mass. Recent adiabatic mass-loss models suggest a new approach to simulate the formation of these binary systems, in which the former donor stars (now observed as the stripped sdO stars) may have attained a more evolved stage as an RGB or AGB star.

Our multiyear spectroscopic investigation has revealed the orbital solutions for five key systems, and this information will complement future FUV observations to constrain the helium stars' masses, atmospheric properties, and compositions. This is a vital step in painting a complete evolutionary portrait of the lives of these binary systems.

This work is based on observations obtained at the Cerro Tololo Inter-American Observatory, NSF's NOIRLab (NOIRLab Prop. IDs 2019A-5152 and 2020A-5169; PI: L. Wang), which is managed by the Association of Universities for Research in Astronomy (AURA) under a cooperative agreement with the National Science Foundation. We thank the members of the SMARTS consortium, Todd Henry, Hodari James, Wei-Chun Jao, and Leonardo Paredes, for their effort in operating the 1.5 m telescope and CTIO staff members Rodrigo Hinojosa and Roberto Aviles for carrying out the observations. We acknowledge an anonymous referee for his or her constructive comments to improve the manuscript. This work was supported by the National Natural Science Foundation of China under program Nos. 12103085, 12090040, and 12090043. The work was also supported by the U.S. National Science Foundation under grant No. AST-1908026. This research is based on observations made with the NASA/ESA Hubble Space Telescope obtained from the Space Telescope Science Institute, which is operated by the Association of Universities for Research in Astronomy, Inc., under NASA contract NAS 5-26555. These observations are associated with program HST-GO-15659. Institutional support was provided by the GSU College of Arts and Science. This work has made use of the SIMBAD database, operated at CDS, Strasbourg, France.

Facility: CTIO:1.5 m.

Appendix A
RV Corrections

Long-term variations in the spectra resulted in measured RVs that appear to show systemic shifts in all five target stars on a timescale of about a year. Thus, we removed such an effect from the measured RVs before obtaining the orbital solutions. Taking the star HD 113120 as an example, Figure A1 shows a time plot of RVs measured from Hα following the procedures described in Section 3.1. Measurements made from the spectra on the nights after HJD 2,458,800 displayed an increasing trend in the RVs (black). We corrected such shifts by dividing the data set into three subsets based on the dates, i.e., spectra observed before HJD 2,458,800 (set 1), between HJD 2,458,800 and 2,459,000 (set 2), and after HJD 2,459,000 (set 3), and then we made a preliminary circular orbital fit to the measured RVs in set 1 (with the most observations) to obtain the systemic velocity γ_1. We then applied the circular orbital fits to RVs in set 2 (set 3) by fixing the P and K_1 parameters obtained from the circular fit from set 1 to update the systemic velocities γ_2 (γ_3). The difference between the systemic velocities $\Delta\gamma = \gamma_1 - \gamma_2$ ($\Delta\gamma = \gamma_1 - \gamma_3$) indicates the deviation of the measured RVs from those in set 1. We applied this difference to the RVs in set 2 (set 3) to correct for any systematic shifts. The corrected RVs of HD 113120 are shown in blue in Figure A1. Table A1 lists the number of

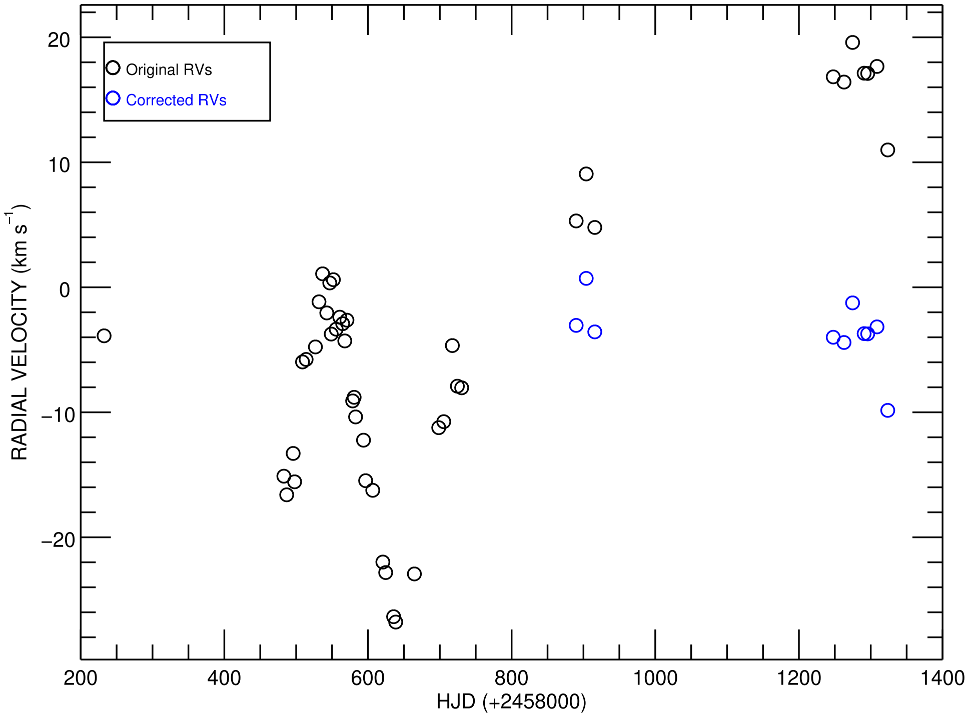

Figure A1. Measured RVs from the Hα profiles of HD 113120. Long-term variations resulted in shifts appearing in the measured RVs obtained after HJD 2,458,800 (black). Corrected RVs are shown in blue.

Table A1
RV Corrections

Data Subset	No. of Observations	γ (km s^{-1})	$\Delta\gamma$ (km s^{-1})
		HD 113120	
1	34	−13.49	…
2	3	−5.14	−8.36
3	7	7.34	−20.84
		HD 137387[a]	
1	26	2.65	…
2	3	−3.85	6.50
3	12	−6.45	9.10
		HD 152478	
1	32	5.68	…
2	4	13.37	−7.69
3	13	16.40	−10.72
		HD 157042	
1	31	1.56	…
2	4	−3.70	5.26
3	12	6.74	−5.18
		HD 157832	
1	30	18.02	…
2	7	23.32	−5.29
3	10	20.88	−2.86

Note.

[a] The relative systemic velocity for each data subset was obtained from the orbital solution of RVs measured by cross-correlating the observed spectra with the coadded mean spectrum of the He I λ5875 profile.

spectra in each of the subsets, the γ velocity obtained from the orbital fitting of each subset for each target star, and the correction factors $\Delta\gamma$ applied to the associated RVs in each subset.

Appendix B
Other RV Measurements

We made a number of ancillary RV measurements beyond the basic sets that were made of the Hα profiles (or He I λ5875 profiles for HD 137387) as described in Section 3. No corrections of long-term variations were applied to these measurements. Here we list the RV shifts measured from other lines for HD 113120 (Table B1), HD 137387 (Table B3), HD 152478 (Table B2), HD 157042 (Table B2), and HD 157832 (Table B3). These are plotted against orbital phase (from Section 3) in Figure B2 (HD 113120), Figure B3 (HD 152478, HD 157042, HD 157832), and Figure B4 (HD 157832). Figure B1 shows an episode of blue wing variability in the Hα line of HD 157832 that influenced the measured RVs.

Table B1
Relative RVs for HD 113120

Date (HJD−2,400,000)	$V_{\mathrm{H}\beta}$[a] (km s^{-1})	σ (km s^{-1})	$V_{\mathrm{Fe\,II}}$[b] (km s^{-1})	σ (km s^{-1})	$V_{\mathrm{Fe\,II}}$[c] (km s^{-1})	σ (km s^{-1})	$V_{\mathrm{Fe\,II}}$[d] (km s^{-1})	σ (km s^{-1})
58,482.8629	−5.4	0.7	−6.2	0.7	−0.7	0.3	−7.5	0.5
58,486.8532	−4.0	0.7	−1.3	0.4	−2.0	0.4	−9.1	0.4
58,495.8407	−2.1	0.7	−2.3	0.4	−1.3	0.4	6.8	0.4
58,497.8571	−0.5	0.6	0.6	0.4	0.1	0.4	−3.4	0.3
58,508.8668	0.5	0.6	1.7	0.4	1.8	0.4	10.5	0.3

Notes.

[a] The RVs were measured for the Hβ profiles by calculating the wing bisectors of the CCFs of the observed spectra with the coadded mean spectrum.

[b] The Fe II $\lambda\lambda$5276, 5316 RVs were measured together for these profiles that were recorded in the same echelle order.

[c] The Fe II $\lambda\lambda$5316, 5362 RVs were measured together for these profiles in the same echelle order.

[d] Fe II λ8451.

(This table is available in its entirety in machine-readable form.)

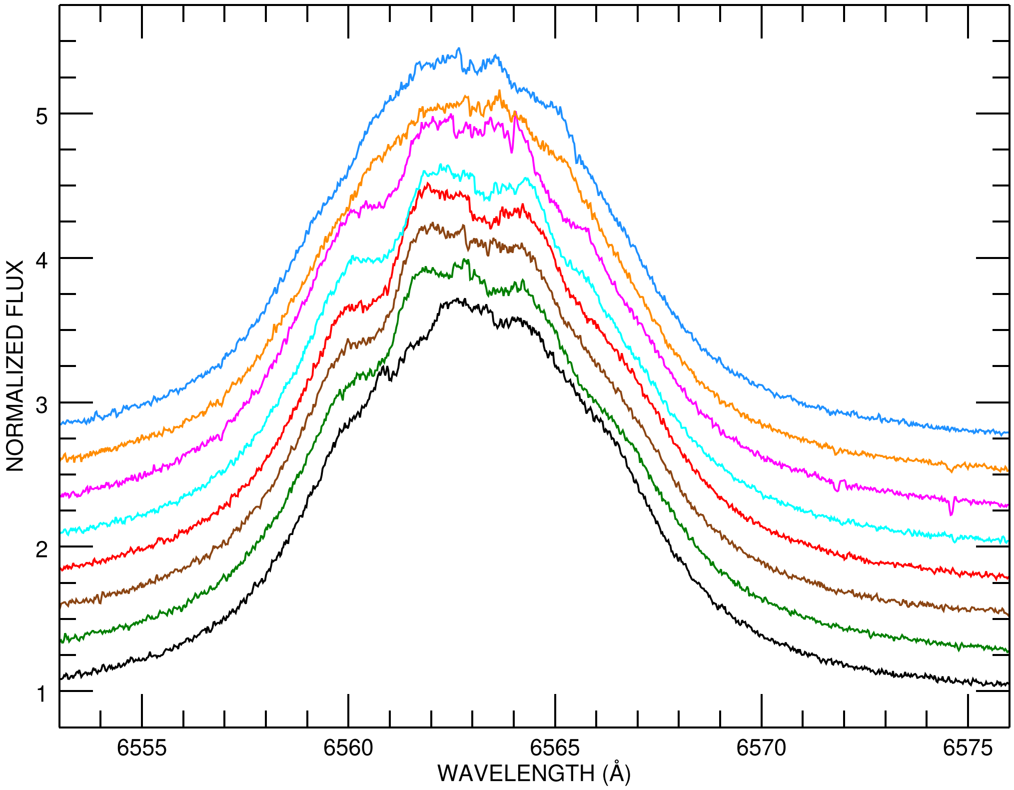

Figure B1. The Hα profiles that were omitted in the orbital fit for HD 157832. The RVs measured from the seven spectra displayed a significant deviation from the derived orbital fit, and these spectra showed a steep drop in intensity in the blue wing of the peak profile. These include observations made on the nights of HJD 2,458,635 (green), HJD 2,458,637 (brown), HJD 2,458,638 (red), HJD 2,458,650 (cyan), HJD 2,458,653 (magenta), HJD 2,458,664 (orange), and HJD 2,458,667 (blue). The spectrum observed on the night of HJD 2,458,625 with a measured RV in accord with the orbital solution is plotted in black for comparison.

Table B2
RVs for HD 152478 and HD 157042 from Hβ

Star Name	Date (HJD−2,400,000)	$V_{\mathrm{H}\beta}$[a] (km s^{-1})	σ (km s^{-1})
152478	58,536.8773	−4.2	2.9
152478	58,538.8683	−0.7	0.8
152478	58,540.8518	−2.1	0.5
152478	58,545.8775	−0.9	0.6
152478	58,547.8603	−0.1	0.5

Note.

[a] The RVs were measured from two adjacent echelle spectral orders that recorded Hβ, and the mean values of these measurements and their associated uncertainties are given here.

(This table is available in its entirety in machine-readable form.)

Table B3
RVs for HD 137387 and HD 157832

Star Name	Date (HJD−2,400,000)	$V_{\mathrm{H}\beta}$ λ4861 (km s^{-1})	$V_{\mathrm{He\ I}}$ (a) λ4713 (km s^{-1})	$V_{\mathrm{He\ I}}$ (b) λ4921 (km s^{-1})	$V_{\mathrm{He\ I}}$ (c) λ5015 (km s^{-1})	$V_{\mathrm{Fe\ II}}$ (d) λ5197 (km s^{-1})	$V_{\mathrm{Fe\ II}}$ (e) λ5234 (km s^{-1})	$V_{\mathrm{Fe\ II}}$ (f) λ5276 (kms^{-1})	$V_{\mathrm{Fe\ II}}$ (g) λ6456 (km s^{-1})	$V_{\mathrm{He\ I}}$ (h) λ6678 (km s^{-1})	$V_{\mathrm{He\ I}}$ (i) λ7065 (km s^{-1})	$V_{\mathrm{O\ I}}$ (j) λ8446 (km s^{-1})	$V_{\mathrm{Ca\ II}}$ (k) λ8542 (km s^{-1})
137387	58,496.8656	11.0 ± 0.6	−15.3 ± 0.8	22.8 ± 0.3	−32.5 ± 1.1	⋯	⋯	⋯	⋯	21.7 ± 0.5	34.2 ± 0.4	⋯	⋯
137387	58,509.8566	3.9 ± 1.1	−16.8 ± 0.6	4.2 ± 0.4	−16.5 ± 0.7	⋯	⋯	⋯	⋯	13.5 ± 1.4	44.8 ± 0.6	⋯	⋯
137387	58,526.8796	−34.6 ± 1.1	−81.6 ± 0.8	−17.1 ± 0.7	−68.9 ± 0.8	⋯	⋯	⋯	⋯	−22.4 ± 1.1	37.8 ± 0.3	⋯	⋯
137387	58,539.8429	−13.0 ± 0.6	−30.3 ± 0.5	1.3 ± 0.4	−20.5 ± 1.1	⋯	⋯	⋯	⋯	21.8 ± 1.1	74.3 ± 0.5	⋯	⋯
137387	58,540.7978	−6.1 ± 0.7	−18.8 ± 0.6	24.6 ± 0.5	−33.3 ± 1.0	⋯	⋯	⋯	⋯	14.4 ± 0.5	103.8 ± 0.6	⋯	⋯

Notes. HD 137387: RVs were measured from the broad CCF wings by cross-correlating the observed spectra with the coadded mean spectrum. RVs were measured over the wavelength range of 4852−4866 for Hβ; 4704−4724 Å for He I λ4713 (a); 4910−4933 Å for He I λ4921 (b); 5007−5024 Å for He I λ5015 (c); 6662−6693 Å for He I λ6678 (h); and 7058−7077 Å for He I λ7065 (i). HD 157832: RVs were measured using CCFs for the He I and metallic line profiles. CCF peak velocities were determined for He I λ4921 (b) (over the wavelength range of 4915−4930 Å), λ5015 (c) (measured together with λ5020 in the same echelle spectral order over the wavelength range of 5012−5026 Å), Fe II including λ5197 (d) (over the wavelength range of 5191−5205 Å), λ5234 (e) (over the range of 5227−5243 Å), λ5276 (f) (5268−5293 Å), and O I λ8446 (j) (over the range of 8409−8489 Å). CCF wing velocities were measured for Fe II λ6456 (g) (over the wavelength range of 6404−6464 Å) and Ca II λ8542 (k) (over the range of 8534−8623 Å). This table is available in its entirety in machine-readable form. The first five entries are shown here for guidance regarding its form and content.

(This table is available in its entirety in machine-readable form.)

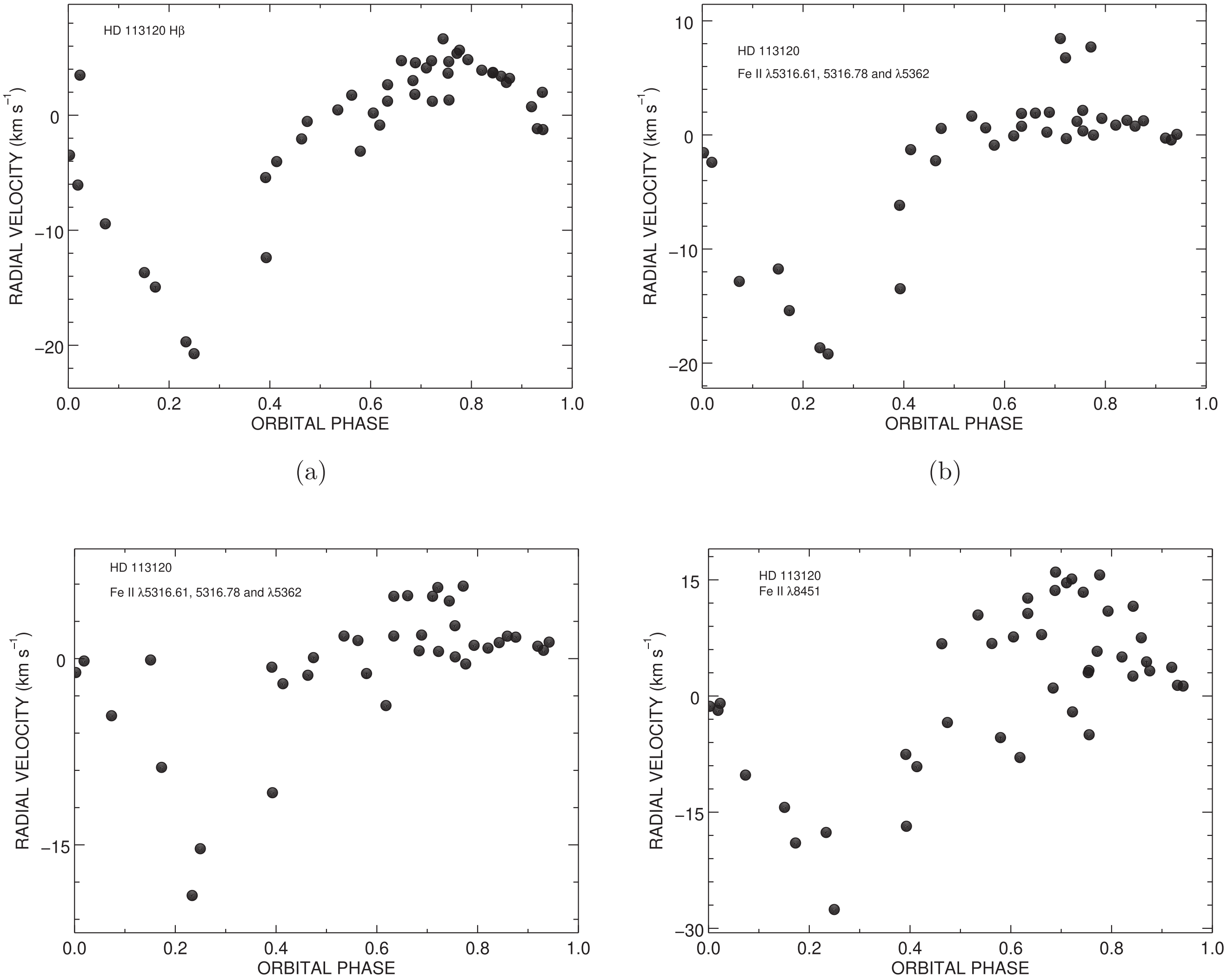

(a)

(b)

(c)

(d)

Figure B2. The RV curves of HD 113120 for Hβ (panel (a)), Fe II λ5276, 5316 (panel (b); all line features were measured together in the same echelle spectral order using the CCF approach), Fe II $\lambda\lambda$ 5316, 5362 (panel (c); all line features were measured together in the same echelle spectral order), and Fe II λ8451 (panel (d)), plotted for phases from the ephemeris reported in Table 3.

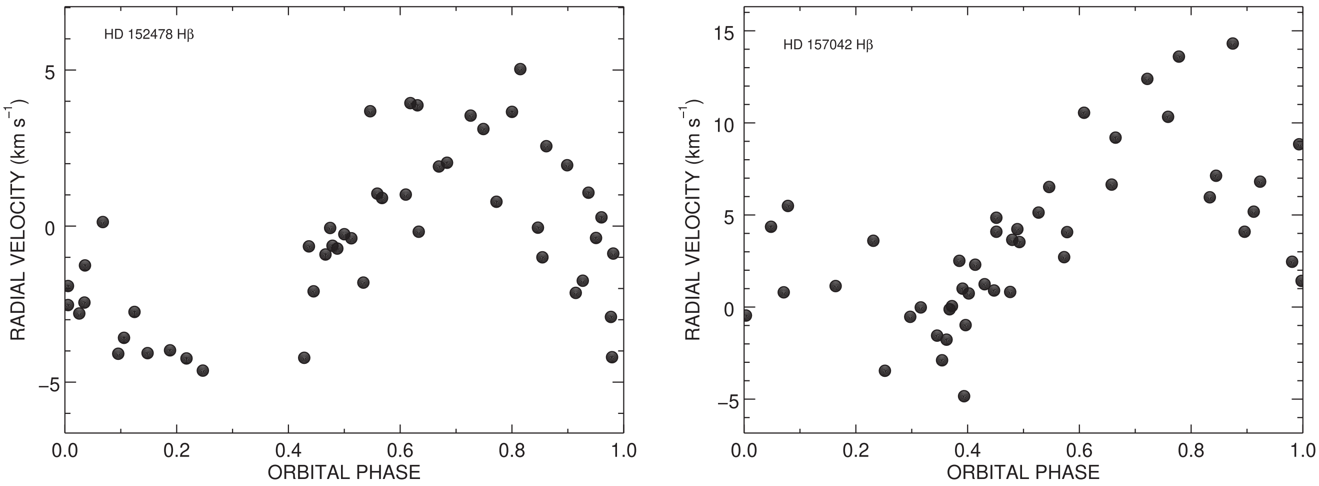

(a) HD 152478 (b) HD 157042

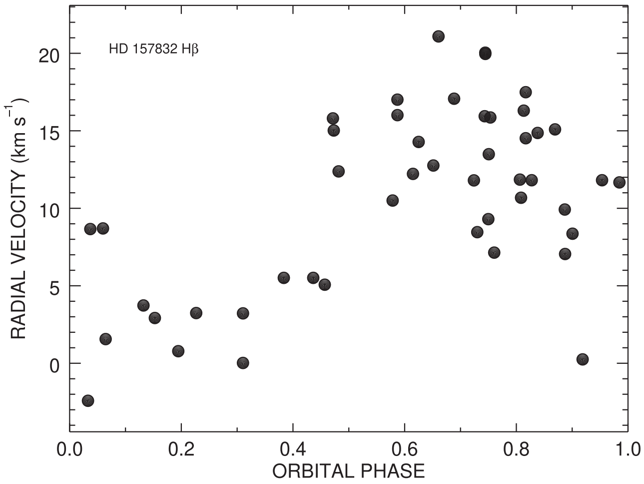

(c) HD 157832

Figure B3. The RV curves from Hβ for the Be binary systems HD 152478 (panel (a)), HD 157042 (panel (b)), and HD 157832 (panel (c)). The relative RVs of the Be stars HD 152478 and HD 157042 were determined from the peak locations of the CCFs constructed by cross-correlating the observed spectra with the coadded mean Hβ profile. Alternatively, the absolute Hβ velocities of HD 157832 were measured directly from the wings using the bisector technique from Shafter et al. (1986). The phases are obtained from the ephemeris reported in Table 5 for HD 152478 (Table 6 for HD 157042 and Table 7 for HD 157832).

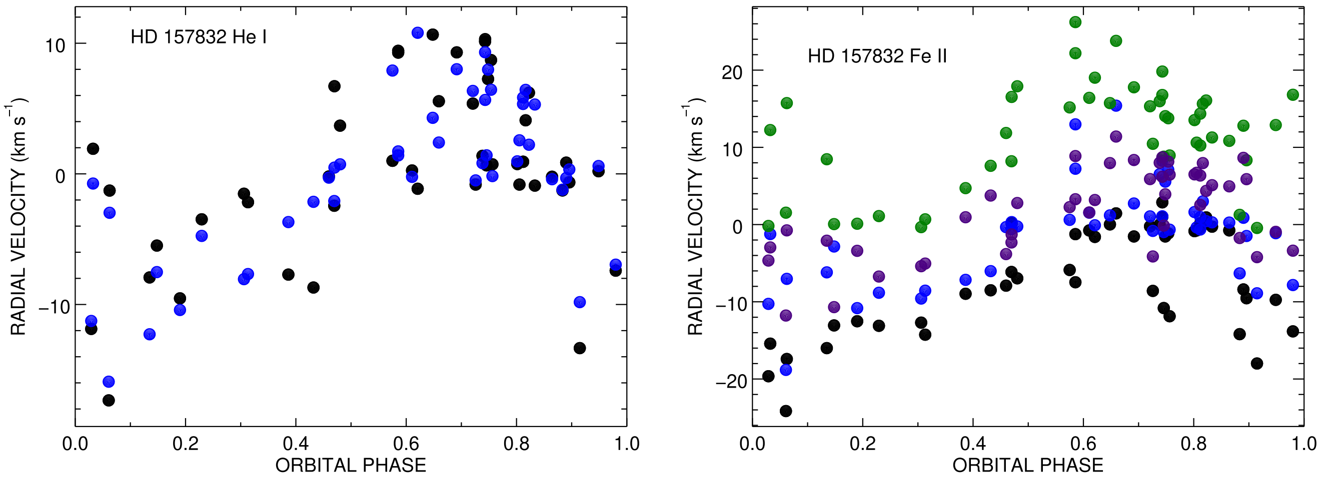

(a) He I

(b) Fe II

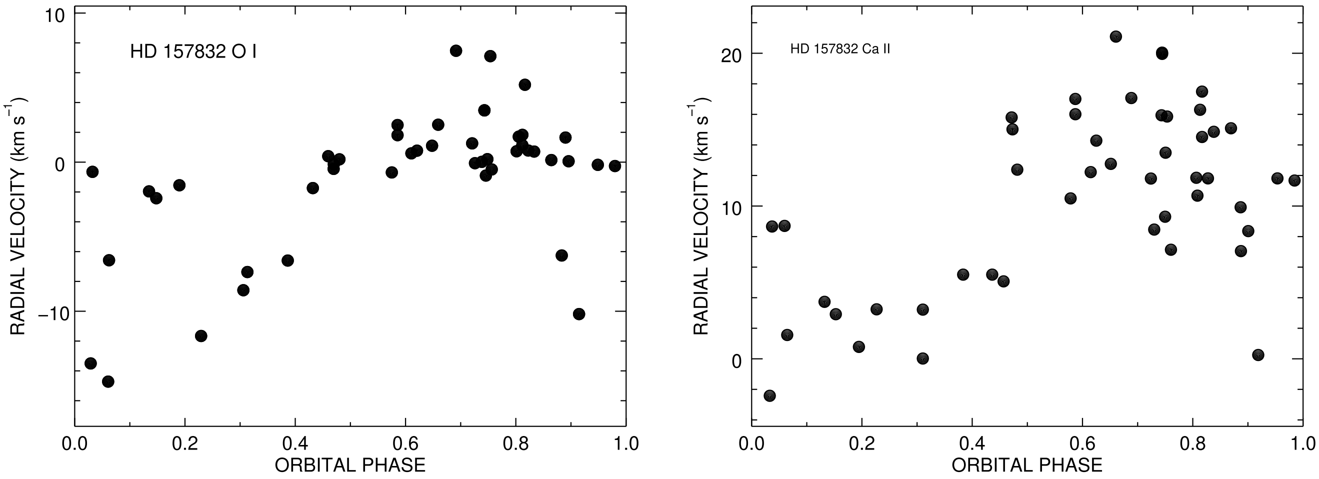

(c) O I

(d) Ca II

Figure B4. The RV plots of the Be star HD 157832 measured from He I and metallic lines, plotted from the ephemeris reported in Table 7. The relative RVs of these profiles were determined from the peak location of the calculated CCFs of observed spectra with the coadded mean spectrum of the associated profile, except in the case of the Fe II λ6456 and Ca II $\lambda\lambda$8542, 8600 profiles, in which the RVs were measured from the CCF wings using the bisector technique. Panel (a): RVs for He I λ4921 (black). Velocities were measured for both the He I λ5015 and Fe II λ5020 profiles together in the same echelle spectral order (blue). Panel (b): RVs for Fe II λ5197 (black), λ5234 (blue), $\lambda\lambda$5276, 5284 (green), and λ6456 (purple). Panel (c): RVs for O I λ8446. Panel (d): RVs for Ca II $\lambda\lambda$8542, 8600.

Appendix C
Equivalent Width Measurements

Equivalent width (W_λ) values were measured over the Hα, Hβ, and He I profiles, the selected spectral ranges for each measured profile are given in Table C1, and the W_λ measurements are collected in Table C2. Subsets of these measurements are plotted in Figures C1 and C2.

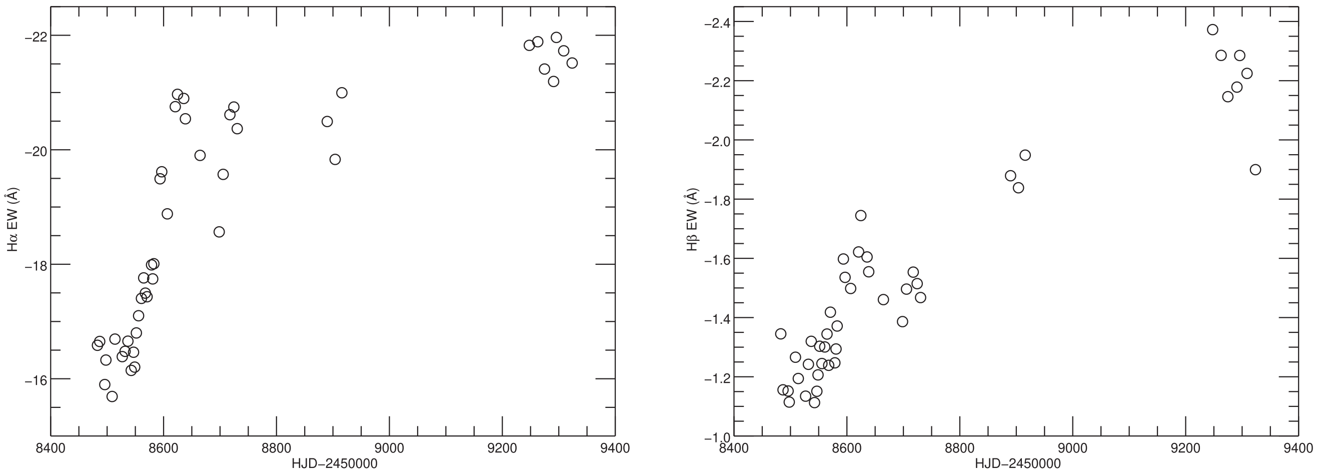

(a) Hα profiles

(b) Hβ profiles

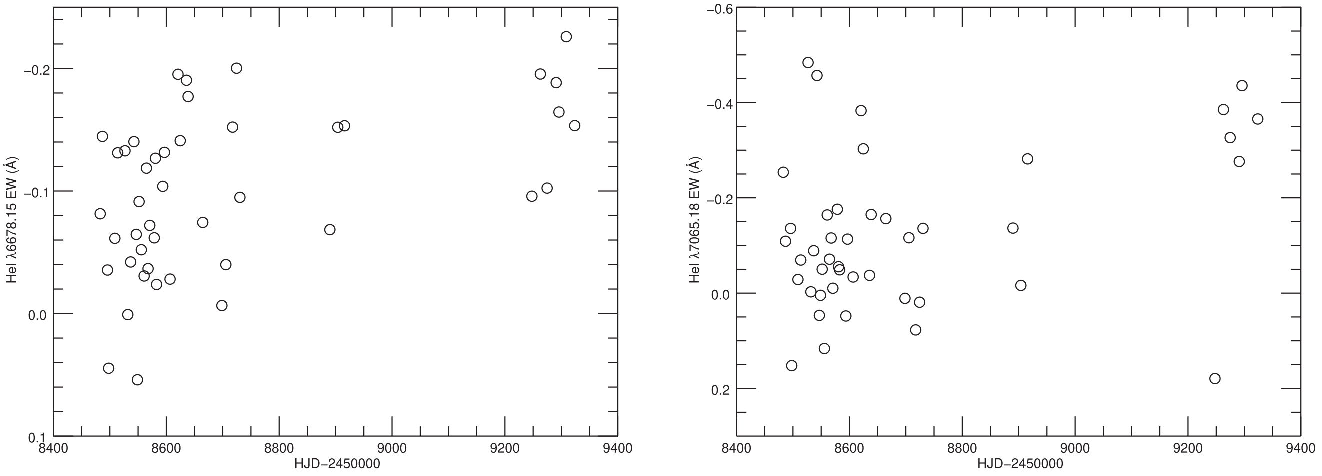

(c) He I λ6678 profiles

(d) He I λ7065 profiles

Figure C1. Time plot of W_λ measured for Hα (panel (a)), Hβ (panel (b)), He I λ6678 (panel (c)), and He I λ7065 (panel (d)) for HD 113120.

Table C1
Wavelength Ranges for Equivalent Width Measurements

Star Name	$W_{\mathrm{H}\alpha}$ (Å)	$W_{\mathrm{H}\beta}$ (Å)	$W_{\mathrm{He\ I}}$(λ4921) (Å)	$W_{\mathrm{He\ I}}$(λ5015) (Å)	$W_{\mathrm{He\ I}}$(λ5875) (Å)	$W_{\mathrm{He\ I}}$(λ6678) (Å)	$W_{\mathrm{He\ I}}$(λ7065) (Å)	$W_{\mathrm{Ca\ II}}$(λ8542) (Å)
113120	6551−6577	4857−4866	⋯	⋯	⋯	6675−6685	7054−7069	⋯
137387	6552−6578	4855−4871	4914−4931	5007−5020	5868−5885	6667−6690	7053−7075	8535−8561
152478	6551−6577	4867−4871	4913−4931	⋯	⋯	6666−6689	7055−7076	⋯
157042	6551−6574	4866−4872	4914−4929	⋯	⋯	6667−6688	7055−7075	⋯
157832	6550−6577	4856−4866	⋯	⋯	⋯	⋯	⋯	⋯

Table C2
Equivalent Width Measurements

Star Name	Date (HJD−2400000)	$W_{\mathrm{H}\alpha}$ (Å)	$W_{\mathrm{H}\beta}$ (Å)	$W_{\text{He I}}(\lambda4921)$ (Å)	$W_{\text{He I}}(\lambda5015)$ (Å)	$W_{\text{He I}}(\lambda5875)$ (Å)	$W_{\text{He I}}(\lambda6678)$ (Å)	$W_{\text{He I}}(\lambda7065)$ (Å)	$W_{\text{Ca II}}(\lambda8542)$ (Å)
113120	58,482.8629	-16.584 ± 0.025	-1.345 ± 0.028	⋯	⋯	⋯	-0.081 ± 0.011	-0.254 ± 0.015	⋯
113120	58,486.8532	-16.651 ± 0.026	-1.156 ± 0.025	⋯	⋯	⋯	-0.145 ± 0.010	-0.109 ± 0.016	⋯
113120	58,495.8407	-15.899 ± 0.025	-1.152 ± 0.024	⋯	⋯	⋯	-0.036 ± 0.010	-0.136 ± 0.018	⋯
113120	58,497.8571	-16.327 ± 0.040	-1.115 ± 0.042	⋯	⋯	⋯	0.045 ± 0.023	0.152 ± 0.036	⋯
113120	58,508.8668	-15.690 ± 0.025	-1.266 ± 0.028	⋯	⋯	⋯	-0.061 ± 0.011	-0.029 ± 0.020	⋯

(This table is available in its entirety in machine-readable form.)

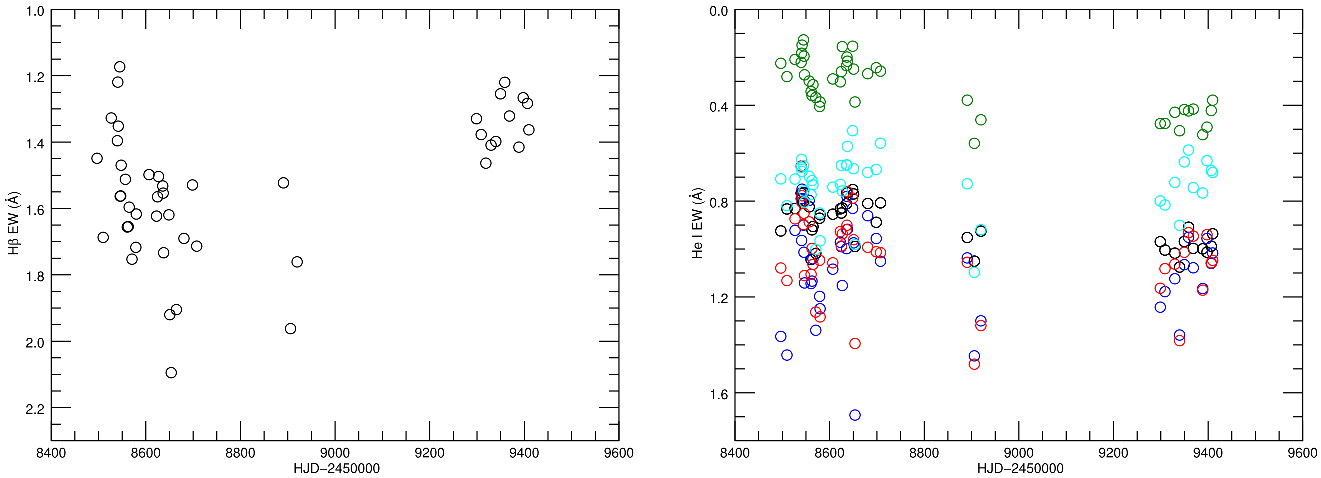

(a) Hβ profiles (b) He I profiles

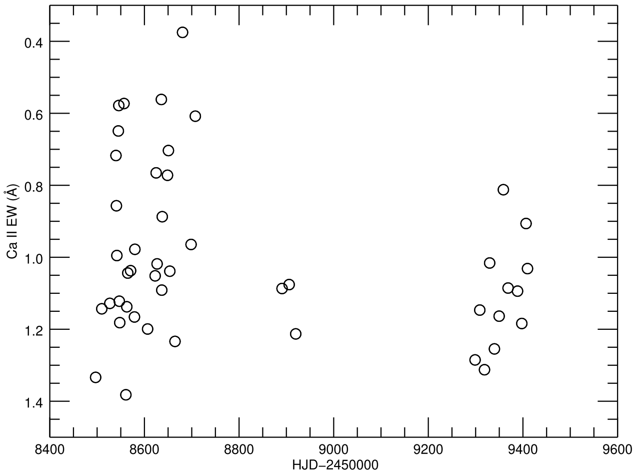

(c) Ca II λ8542 profiles

Figure C2. Time plot of W_λ for Hβ (panel (a)), He I (panel (b)), and Ca II λ8542 (panel (c)) for HD 137387. Measured W_λ values for He I λ4921 (black), λ5015 (green), λ5875 (blue), λ6678 (red), and λ7065 (cyan) are shown in panel (b).

Appendix D
Notes on Individual Stars

HD 113120 (LS Mus). Hohle et al. (2010) applied a model fit to derive the stellar parameters and estimated that the Be star has a mass of $M_{\rm Be} = 8.5 \pm 0.5\ \mathcal{M}_\odot^{\rm N}$. If so, then the sdO star mass is $1.30 \pm 0.8\ \mathcal{M}_\odot^{\rm N}$, i.e., just below the Chandrasekhar limit. Zorec et al. (2016) reported that the rapidly rotating Be star has $V \sin i = 339 \pm 30$ km s^{-1}, $T_{\rm eff} = 22.8 \pm 0.7$ kK, $\log g = 3.69 \pm 0.44$ (cm s^{-2}), and $\log L_{\rm Be} = 3.91 \pm 0.04\ \mathcal{L}_\odot^{\rm N}$. The subdwarf companion of this star was first detected by Wang et al. (2018) through a cross-correlation technique using FUV spectra from IUE and later confirmed by Wang et al. (2021) from HST/STIS observations. Based upon the FUV spectroscopic analysis, Wang et al. (2021) reported that the sdO star has an estimated $T_{\rm eff} = 45$ kK, $f_{\rm sdO}/f_{\rm Be} = 4.1\% \pm 0.9\%$ in the FUV, $R_{\rm sdO} = 0.30 \pm 0.10\ \mathcal{R}_\odot^{\rm N}$, and $\log L_{\rm sdO} = 2.52\ \mathcal{L}_\odot^{\rm N}$. Through an SED fitting to the observations, they suggested that the Be star has a size of $R_{\rm Be} = 4.11 \pm 0.79\ \mathcal{R}_\odot^{\rm N}$. Brandt (2021) cross-calibrated the Hipparcos and Gaia EDR3 surveys and identified this star as an astrometric accelerating star with a faint companion.

HD 137387 (κ Aps). Levenhagen & Leister (2006) derived an age estimation of $\log {\rm Age(yr)} = 7.29$ based on models. Zorec et al. (2016) reported that the Be component has $V \sin i = 250 \pm 21$ km s^{-1}, $T_{\rm eff} = 24.0 \pm 2.6$ kK, $\log g = 4.01 \pm 0.23$ (cm s^{-2}), and $\log L_{\rm Be} = 4.05 \pm 0.09\ \mathcal{L}_\odot^{\rm N}$. Wang et al. (2021) confirmed the detection of the hot subdwarf companion of this system and reported that the sdO star has $T_{\rm eff} = 40$ kK, $f_{\rm sdO}/f_{\rm Be} = 3.2\% \pm 0.3\%$ in the FUV, $R_{\rm sdO} = 0.44 \pm 0.06\ \mathcal{R}_\odot^{\rm N}$, and $\log L_{\rm sdO} = 2.65\ \mathcal{L}_\odot^{\rm N}$.

HD 152478 (V846 Ara). Levenhagen & Leister (2006) derived an age of $\log {\rm Age(yr)} = 7.34$. Hohle et al. (2010) derived a mass of $M_{\rm Be} = 6.3 \pm 0.4\ \mathcal{M}_\odot^{\rm N}$. The Be component has estimates of $V \sin i = 295 \pm 18$ km s^{-1}, $T_{\rm eff} = 19.8 \pm 0.6$ kK, $\log g = 3.74 \pm 0.19$ (cm s^{-2}), and $\log L_{\rm Be} = 3.09 \pm 0.02\ \mathcal{L}_\odot^{\rm N}$ from Zorec et al. (2016). Wang et al. (2021) reported that the sdO companion has $T_{\rm eff} = 42$ kK, $f_{\rm sdO}/f_{\rm Be} = 4.9\% \pm 0.3\%$ in the FUV, $R_{\rm sdO} = 0.27 \pm 0.04\ \mathcal{R}_\odot^{\rm N}$, and $L_{\rm sdO} = 2.31\ \mathcal{L}_\odot^{\rm N}$.

HD 157042 (ι Ara). Arcos et al. (2018) derived the stellar parameters for the Be component of $T_{\rm eff} = 22 \pm 0.22$ kK, $\log g = 3.90 \pm 0.04$ (cm s^{-2}), $R = 5.17 \pm 0.1$ $\mathcal{R}_\odot^{\rm N}$, and $V \sin i = 280 \pm 6$ km s^{-1} from the Be Stars Observation Survey. Wang et al. (2021) reported the determination of the atmospheric properties of the sdO companion of $T_{\rm eff} = 33.8$ kK, $f_{\rm sdO}/f_{\rm Be} = 2.6\% \pm 0.3\%$ in the FUV, $R_{\rm sdO} = 0.61 \pm 0.09$ $\mathcal{R}_\odot^{\rm N}$, and $L_{\rm sdO} = 2.64$ $\mathcal{L}_\odot^{\rm N}$.

HD 157832 (V750 Ara). This star is identified as a γ Cas analog star, which displays photometric variations in TESS light curves (Nazé et al. 2020). Nazé et al. (2022) confirmed this star's hard X-ray emission features from recent space observations. A marginal signature of an sdO companion star was detected from IUE FUV spectroscopy by Wang et al. (2018), but such a feature was not found in the HST spectra by Wang et al. (2021).

ORCID iDs

Luqian Wang (王璐茜) https://orcid.org/0000-0003-4511-6800
Douglas R. Gies https://orcid.org/0000-0001-8537-3583
Geraldine J. Peters https://orcid.org/0000-0003-4202-269X
Zhanwen Han https://orcid.org/0000-0001-9204-7778

References

Abt, H. A., & Levy, S. G. 1978, ApJS, 36, 241
Aguilera-Dena, D. R., Müller, B., Antoniadis, J., et al. 2023, A&A, 671, A134
Arcos, C., Kanaan, S., Chávez, J., et al. 2018, MNRAS, 474, 5287
Bagnuolo, W. G., Jr., Gies, D. R., Hahula, M. E., Wiemker, R., & Wiggs, M. S. 1994, ApJ, 423, 446
Bjorkman, K. S., Miroshnichenko, A. S., McDavid, D., & Pogrosheva, T. M. 2002, ApJ, 573, 812
Brandt, T. D. 2021, ApJS, 254, 42
Carrier, F., Burki, G., & Burnet, M. 2002, A&A, 385, 488
Chojnowski, S. D., Labadie-Bartz, J., Rivinius, T., et al. 2018, ApJ, 865, 76
de Mink, S. E., Langer, N., Izzard, R. G., Sana, H., & de Koter, A. 2013, ApJ, 764, 166
Ekström, S., Meynet, G., Maeder, A., & Barblan, F. 2008, A&A, 478, 467
Ge, H., Webbink, R. F., Chen, X., & Han, Z. 2020, ApJ, 899, 132
Gies, D. R., Bagnuolo, W. G., Jr., Ferrara, E. C., et al. 1998, ApJ, 493, 440
Gies, D. R., & Wang, L. 2020, ApJL, 898, L44
Götberg, Y., de Mink, S. E., Groh, J. H., Leitherer, C., & Norman, C. 2019, A&A, 629, A134
Granada, A., Ekström, S., Georgy, C., et al. 2013, A&A, 553, A25
Grundstrom, E. D. 2007, PhD thesis, Georgia State Univ.
Hanuschik, R. W., Hummel, W., Sutorius, E., Dietle, O., & Thimm, G. 1996, A&AS, 116, 309
Harmanec, P., Božić, H., Koubský, P., et al. 2022, A&A, 666, A136
Harmanec, P., Bozić, H., Percy, J. R., et al. 2002, A&A, 387, 580
Harmanec, P., Habuda, P., Štefl, S., et al. 2000, A&A, 364, L85
Harmanec, P., Lipták, J., Koubský, P., et al. 2020, A&A, 639, A32
Hinkle, K. H., Wallace, L., & Livingston, W. 2003, AAS Meeting Abstracts, 203, 38.03
Hohle, M. M., Neuhäuser, R., & Schutz, B. F. 2010, AN, 331, 349
Iglesias-Marzoa, R., López-Morales, M., & Jesús Arévalo Morales, M. 2015, PASP, 127, 567
Jilinski, E., Ortega, V. G., Drake, N. A., & de la Reza, R. 2010, ApJ, 721, 469
Klement, R., Baade, D., Rivinius, T., et al. 2022a, ApJ, 940, 86
Klement, R., Schaefer, G. H., Gies, D. R., et al. 2022b, ApJ, 926, 213
Kolbas, V., Pavlovski, K., Southworth, J., et al. 2015, MNRAS, 451, 4150
Koubský, P., Kotková, L., Kraus, M., et al. 2014, A&A, 567, A57
Koubský, P., Kotková, L., Votruba, V., Šlechta, M., & Dvořáková, Š. 2012, A&A, 545, A121
Lanz, T., & Hubeny, I. 2003, ApJS, 146, 417
Lanz, T., & Hubeny, I. 2007, ApJS, 169, 83
Laplace, E., Justham, S., Renzo, M., et al. 2021, A&A, 656, A58
Levenhagen, R. S., & Leister, N. V. 2006, MNRAS, 371, 252
Lopes de Oliveira, R., & Motch, C. 2011, ApJL, 731, L6
Meilland, A., Stee, P., Vannier, M., et al. 2007, A&A, 464, 59
Meynet, G., Ekström, S., Maeder, A., & Barblan, F. 2007, in ASP Conf. Ser. 361, Active OB-Stars: Laboratories for Stellar and Circumstellar Physics, ed. A. T. Okazaki, S. P. Owocki, & S. Stefl (San Francisco, CA: ASP), 325
Mourard, D., Monnier, J. D., Meilland, A., et al. 2015, A&A, 577, A51
Nazé, Y., Rauw, G., Czesla, S., Smith, M. A., & Robrade, J. 2022, MNRAS, 510, 2286
Nazé, Y., Rauw, G., & Pigulski, A. 2020, MNRAS, 498, 3171
Nemravová, J., Harmanec, P., Koubský, P., et al. 2012, A&A, 537, A59
Panoglou, D., Faes, D. M., Carciofi, A. C., et al. 2018, MNRAS, 473, 3039
Paredes, L. A., Henry, T. J., Quinn, S. N., et al. 2021, AJ, 162, 176
Peters, G. J., Gies, D. R., Grundstrom, E. D., & McSwain, M. V. 2008, ApJ, 686, 1280
Peters, G. J., Pewett, T. D., Gies, D. R., Touhami, Y. N., & Grundstrom, E. D. 2013, ApJ, 765, 2
Peters, G. J., Wang, L., Gies, D. R., & Grundstrom, E. D. 2016, ApJ, 828, 47
Poeckert, R. 1981, PASP, 93, 297
Pols, O. R., Cote, J., Waters, L. B. F. M., & Heise, J. 1991, A&A, 241, 419
Porter, J., & Rivinius, T. 2003, PASP, 115, 1153
Prša, A., Harmanec, P., Torres, G., et al. 2016, AJ, 152, 41
Quirrenbach, A., Bjorkman, K. S., Bjorkman, J. E., et al. 1997, ApJ, 479, 477
Reig, P. 2011, Ap&SS, 332, 1
Rivinius, T., Carciofi, A. C., & Martayan, C. 2013, A&ARv, 21, 69
Rivinius, T., Vanzi, L., Chacon, J., et al. 2012, in ASP Conf. Ser. 464, Circumstellar Dynamics at High Resolution, ed. A. C. Carciofi & T. Rivinius (San Francisco, CA: ASP), 75
Ruždjak, D., Božić, H., Harmanec, P., et al. 2009, A&A, 506, 1319
Schneider, F. R. N., Podsiadlowski, P., & Müller, B. 2021, A&A, 645, A5
Shafter, A. W., Szkody, P., & Thorstensen, J. R. 1986, ApJ, 308, 765
Shao, Y., & Li, X.-D. 2014, ApJ, 796, 37
Shao, Y., & Li, X.-D. 2021, ApJ, 908, 67
Shenar, T., Bodensteiner, J., Abdul-Masih, M., et al. 2020, A&A, 639, L6
Slettebak, A. 1982, ApJS, 50, 55
Stancliffe, R. J., & Eldridge, J. J. 2009, MNRAS, 396, 1699
Temmink, K. D., Pols, O. R., Justham, S., Istrate, A. G., & Toonen, S. 2023, A&A, 669, A45
Tetzlaff, N., Neuhäuser, R., & Hohle, M. M. 2011, MNRAS, 410, 190
Thaller, M. L., Bagnuolo, W. G. J., Gies, D. R., & Penny, L. R. 1995, ApJ, 448, 878
Tokovinin, A., Fischer, D. A., Bonati, M., et al. 2013, PASP, 125, 1336
van Bever, J., & Vanbeveren, D. 1997, A&A, 322, 116
Wang, L., Gies, D. R., & Peters, G. J. 2017, ApJ, 843, 60
Wang, L., Gies, D. R., & Peters, G. J. 2018, ApJ, 853, 156
Wang, L., Gies, D. R., Peters, G. J., et al. 2021, AJ, 161, 248
Zorec, J., Frémat, Y., Domiciano de Souza, A., et al. 2016, A&A, 595, A132